Volume 49
Number 11
7 June 2020
Pages 3235–3718

Chem Soc Rev

Chemical Society Reviews

rsc.li/chem-soc-rev

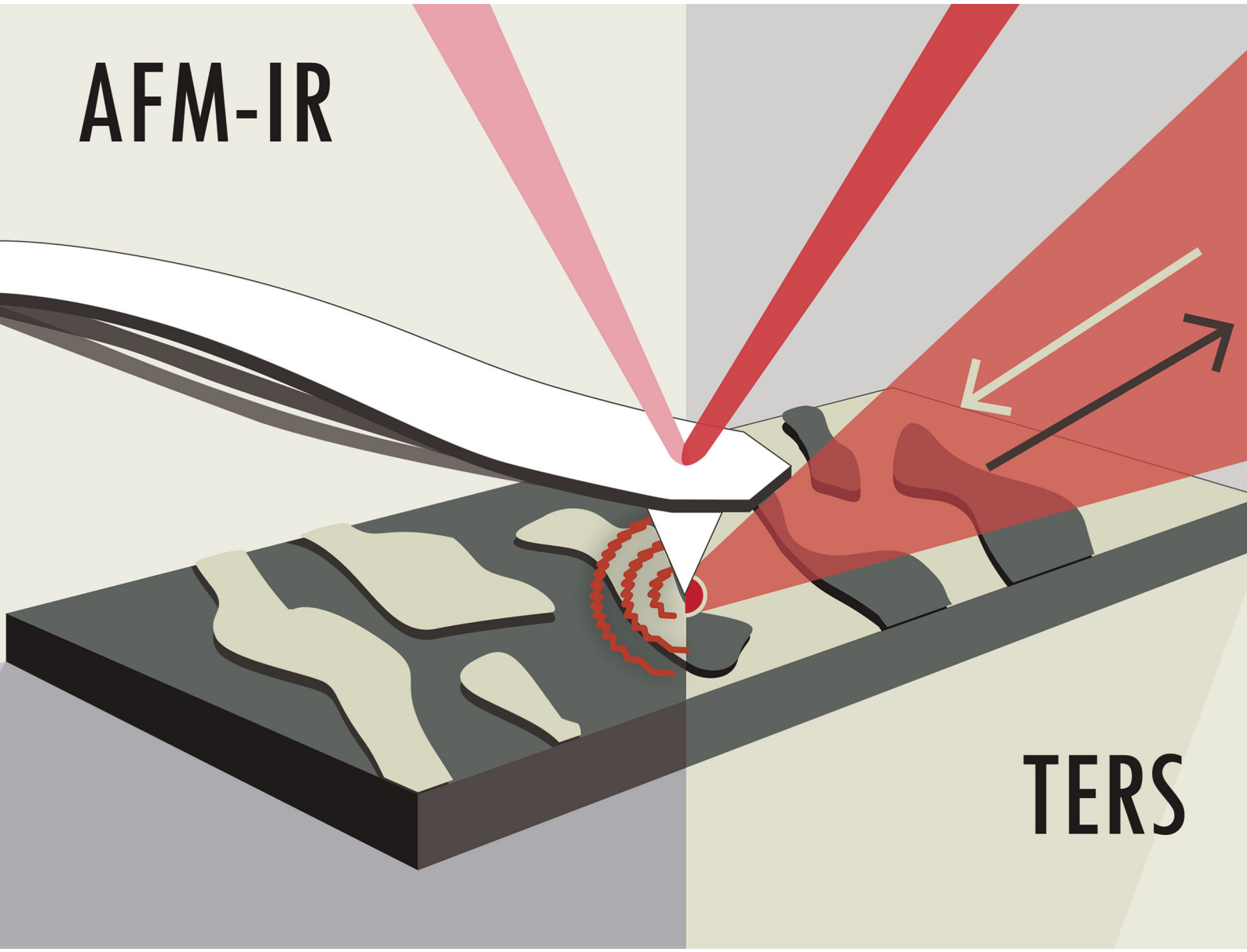

ISSN 0306-0012

ROYAL SOCIETY OF CHEMISTRY

REVIEW ARTICLE

Dmitry Kurouski, Alexandre Dazzi, Renato Zenobi and Andrea Centrone

Infrared and Raman chemical imaging and spectroscopy at the nanoscale

Chem Soc Rev

REVIEW ARTICLE

View Article Online
View Journal | View Issue

Cite this: *Chem. Soc. Rev.*, 2020, **49**, 3315

Infrared and Raman chemical imaging and spectroscopy at the nanoscale

Dmitry Kurouski,*[a] Alexandre Dazzi,*[b] Renato Zenobi*[c] and Andrea Centrone*[d]

The advent of nanotechnology, and the need to understand the chemical composition at the nanoscale, has stimulated the convergence of IR and Raman spectroscopy with scanning probe methods, resulting in new nanospectroscopy paradigms. Here we review two such methods, namely photothermal induced resonance (PTIR), also known as AFM-IR and tip-enhanced Raman spectroscopy (TERS). AFM-IR and TERS fundamentals will be reviewed in detail together with their recent crucial advances. The most recent applications, now spanning across materials science, nanotechnology, biology, medicine, geology, optics, catalysis, art conservation and other fields are also discussed. Even though AFM-IR and TERS have developed independently and have initially targeted different applications, rapid innovation in the last 5 years has pushed the performance of these, in principle spectroscopically complimentary, techniques well beyond initial expectations, thus opening new opportunities for their convergence. Therefore, subtle differences and complementarity will be highlighted together with emerging trends and opportunities.

Received 2nd September 2019

DOI: 10.1039/c8cs00916c

rsc.li/chem-soc-rev

[a] *Department Biochemistry and Biophysics, Texas A&M University, 2128 TAMU, College Station, TX 77843, USA. E-mail: dkurouski@tamu.edu*
[b] *Institut de Chimie Physique, CNRS UMR8000, Université Paris-Saclay, Orsay, France. E-mail: alexandre.dazzi@universite-paris-saclay.fr*
[c] *Department of Chemistry and Applied Biosciences, ETH Zurich, CH-8093 Zurich, Switzerland. E-mail: zenobi@org.chem.ethz.ch*
[d] *Nanoscale Device Characterization Division, Physical Measurement Laboratory, National Institute of Standards and Technology, Gaithersburg, Maryland 20899, USA. E-mail: andrea.centrone@nist.gov*

1. Introduction to IR and Raman spectroscopy, microscopy and nanoscopy

Raman and infrared (IR) spectroscopies measure molecular vibrations and phonons providing rich information on the sample chemical composition, molecular conformation and chemical structure. However, these two methods probe

Dmitry Kurouski

Dmitry Kurouski earned his MS in Biochemistry from Belarusian State University, Belarus and PhD (Distinguished Dissertation) in Analytical Chemistry from SUNY Albany, NY, USA. After a Postdoc in the laboratory of Professor Richard P. Van Duyne at Northwestern University, Dr Kurouski joined Boehringer-Ingelheim Pharmaceuticals, where he worked as Senior Research Scientist. In 2017, Dr Kurouski joined Biochemistry and Biophysics Department of Texas A&M University as Assistant Professor. His research interests are focused on nanoscale characterization of biological and photocatalytic systems using TERS and AFM-IR.

Alexandre Dazzi

Alexandre Dazzi is a tenured Professor of physics at Université Paris-Saclay and works in the Insitut de Chimie Physique. Alexandre does research focused on the infrared and nanoscience domain. After inventing and developing the AFM-IR technique, Alexander has worked to improve AFM-IR instrumentation and focused on bio applications. Now, He has a user facility and collaborates with many groups in different domains like astro-physics, culture heritage, polymer science, microbiology. He was the 2009 recipient of the instrumentation prize from the Societé Francaise Division de Chimie Physique and received the Ernst Abbe Award in 2014 from the New York Microscopical Society.

vibrational states based on physically different mechanisms: IR spectroscopy by measuring light absorption *via* electric dipolar interactions, Raman spectroscopy by measuring inelastically scattered light *via* the sample polarizability tensor. In general, IR spectroscopy is more sensitive to vibrational modes localized on specific chemical groups (typically with strong dipoles) while Raman spectroscopy is more sensitive to collective vibrational modes involving many atoms (typically with large polarizability). Depending on the sample molecular symmetry certain vibrations can be measured only in Raman spectra and are absent in IR spectra or *vice versa*, due to the different selection rules for IR and Raman transitions.[1,2] However, in many cases (molecules with non-center-symmetric point groups) several vibrations can be observed by both techniques, although with considerably different intensities. For example, the spectral intensity of aliphatic groups increases linearly and quadratically with the length of the aliphatic chain in IR and Raman spectra, respectively.[3] As a result, the carbonyl vibration of fatty acids is not evident in Raman, but it is detected in IR spectra. At the same time, Raman is sensitive to conformations of aliphatic chains of fatty acids that cannot be probed by IR. Therefore, in the far-field, macroscale IR and Raman spectroscopies are strongly complimentary and are often used in concert to gain a more complete understanding of the sample composition and molecular structure.[2–4]

The rise of nanotechnology and the desire to investigate the hierarchical structure of biological materials to the finest scale has rendered the characterization of materials and biological samples at the nanoscale a priority. However, the best possible spatial resolution obtainable with conventional IR and Raman microscopies is limited by light diffraction to approximately half of the wavelength of light, *i.e.* 1.5 μm to 10 μm in the IR, and 250 nm to ≈500 nm for Raman, which typically relies on a visible or near-IR laser. Not only the spatial resolution of conventional IR and Raman microscopies is insufficient to capture nanoscale details, the wavelength dependent resolution of IR spectroscopy also makes the comparison of chemical maps obtained with the two techniques somewhat difficult.

The coupling of Raman and IR spectroscopy with Scanning Probe Microscopy (SPM) has provided scientists with a common platform to overcome the limitations imposed by light diffraction, pushing the spatial resolution to the nanoscale and beyond. Here, we review two nanoscale analogs of Raman and IR spectroscopy, namely: tip-enhanced Raman spectroscopy (TERS) and photothermal induced resonance (PTIR), which is also commonly known as AFM-IR in the IR spectral range. Excellent reviews on TERS and AFM-IR and their applications have been published over the last decade;[5–9] here we focus on the most recent advances. In the last 5 years, these techniques have improved at an ever-faster pace, leading to new technical capabilities and better understanding of measurements underlying physical processes which ultimately have fostered ever more applications.

Despite sharing the same scanning probe platform, TERS and AFM-IR have evolved independently and are based on different physical mechanisms. While the SPM tip is the key enabling factor in TERS measurements, details of the dynamics of the sample thermal expansion and of the SPM cantilever oscillation are critical to understand the fine details of AFM-IR spectral intensities. The purpose of this review is to inform the reader of the working principles, discuss the most recent technical advances and compare capabilities of these nanoscale spectroscopic techniques. Particularly, their subtle differences, complementarity and synergies will be highlighted with the aim of identifying a few outstanding challenges that, if overcome, could foster the integration of these, in principle,

Renato Zenobi

Renato Zenobi is Professor of Analytical Chemistry at the Swiss Federal Institute of Technology (ETH) Zurich. After a PhD at Stanford University and postdoctoral appointments at the University of Pittsburgh and at the University of Michigan, he returned to Switzerland in 1992 as a Werner Fellow at EPF Lausanne, where he established his own research group. He became assistant professor at the ETH in 1995 and was promoted to full professor in 2000. Zenobi has made important contributions to the understanding of the ion formation mechanism in matrix-assisted laser desorption/ionization (MALDI) mass spectrometry, to the development of analytical tools for the nanoscale, in particular TERS (tip-enhanced Raman spectroscopy), and to exhaled breath analysis using ambient ionization methods.

Andrea Centrone

Andrea Centrone is Project Leader at the National Institute of Standard and Technology (NIST) Gaithersburg, MD. He obtained a PhD in Materials Engineering from the Polytechnic University of Milan, Italy, working with Professor G. Zerbi. Before joining NIST in 2010, Andrea had two postdoctoral appointments (Rocca Fellow) at the Massachusetts Institute of Technology (MIT). At NIST Andrea is making important contributions to improve PTIR/AFM-IR and other nanoscale techniques and, in collaboration with several groups, to their application in fields such as nano-optics, photovoltaics, nanomedicine, and art conservation. Currently, Andrea aims to further develop these techniques to enable the characterization of quantum materials.

spectroscopically complementary methods. Finally, we will discuss TERS and AFM-IR prospects.

2. AFM-IR: fundamental principles and recent advances

In this section we will discuss the working principles and the physical mechanisms contributing to the AFM-IR signal transduction,[10,11] (Section 2.1), the sample illumination schemes (Section 2.2) alongside the innovations responsible for the recent performance improvements and expanded AFM-IR application space (discussed in Section 3). These innovations resulted in diverse AFM-IR measurements modalities either in contact-mode, *i.e.* ringdown[12] (Section 2.3) and resonance enhanced excitation[13] (Section 2.4), or in tapping-mode *via* heterodyne detection[14–17] or peak force[18] (Section 2.5). The key characteristics of AFM-IR methods are summarized in Table 1.

2.1 AFM-IR signal transduction

AFM-IR[5,6] was developed by Dazzi *et al.*,[12] to fulfill the desire of combining the rich compositional information available from IR spectroscopy with the nanoscale spatial resolution of AFM. AFM-IR instruments consist of a spectrally narrow, pulsed, wavelength-tunable laser source (typically a quantum cascade laser, QCL, or an optical parametric oscillator, OPO), an atomic force microscope and the optics to focus the laser beam around the tip of an AFM cantilever. In contrast to conventional spectroscopic methods, that rely on light-sensitive detectors in the far-field, in AFM-IR the sharp tip of the AFM cantilever mechanically transduces in the near-field the photothermal expansion of the sample. In AFM-IR, the laser illuminates the sample area ($\approx$40 μm diameter) centered around the AFM tip. The parts of the sample absorbing the laser pulses heat up and thermally expand rapidly, within a time frame comparable to the laser pulse length (see Table 1).[10,19] Notably, to first approximation, only the portion of the sample directly beneath the AFM tip pushes the cantilever and contributes to the AFM-IR signal. Since thermal expansion coefficients are small (from $\approx 10^{-6}$ to 10^{-4}), and the temperature rise in the typically sub-μm thick samples is limited (see Table 1);[13] the resulting thermal expansion is very small ($\ll$1 nm)[19] and decays rapidly (from sub ns to few μs, depending on the thickness and thermal conductivity of the sample).[19,20] In AFM-IR, such fast thermal expansion dynamics can be captured directly using fast ($\approx$10 ns response time) custom-made nanophotonic probes[19] (see below), but is too rapid for conventional AFM cantilevers (tens of μs response time).[10] Conventional cantilevers are instead shocked by the expansion and kicked into oscillation akin to a struck tuning fork. The main interest of this approach is due to the amplitude of the induced oscillation (measured by the AFM detector) being directly proportional to the local absorption of the sample.[10,11,19,21,22] AFM-IR absorption spectra are obtained by keeping the AFM tip stationary and sweeping the laser wavelength. AFM-IR absorption maps are obtained illuminating the sample at a fixed wavelength while scanning the AFM tip over the sample.

Dazzi *et al.*[10] established a theoretical framework to describe the AFM-IR signal ($S_{\text{AFM-IR}}$) as a series of multiplicative contributions mirroring the AFM-IR transduction chain: optical energy into absorbed energy, local heat, local thermal expansion, AFM cantilever motion, and AFM detector signal, which we write in the form of Ramer *et al.*:[11]

$$S_{\text{AFM-IR}} \propto H_{\text{AFM}} H_{\text{m}} H_{\text{th}} H_{\text{opt}}(\lambda) I_{\text{inc}}(\lambda) \quad (1)$$

where, λ is the wavelength and (I_{inc}) the intensity of the laser incident power, typically accounted for by the background spectrum. The cantilever contribution (H_{AFM}) depends on the cantilever modal stiffnesses, frequencies, shapes and deflection sensitivity, tip height and cantilever tilt angle. The mechanical contribution (H_{m}) depends on the sample thermal expansion coefficient. The thermal contribution (H_{th}), describes the sample thermalization dynamics as a function of the laser pulse length and sample thermal properties. The optical contribution (H_{opt}) is defined here as the fraction of incident light absorbed by the sample, *i.e.* its absorptance which depends on the sample refractive index $\hat{n}(\lambda) = n(\lambda) + i\kappa(\lambda)$.

Notably, since I_{inc} is determined in a separate background measurement, H_{opt}, is the only factor in eqn (1) comprising the absorption coefficient ($\kappa(\lambda)$) and the only factor that is a function of the wavelength *i.e.* it fully describes AFM-IR spectra apart from a scaling factor. Under the electric dipole approximation (size of the object $\ll$ wavelength and weak absorbers) there is a direct linear relationship between the AFM-IR signal and $\kappa(\lambda)$.[10] Beyond this approximation, which describes most cases, Ramer *et al.* recently demonstrated that even in the worst case scenario, *i.e.* total internal reflection illumination of a thick sample ($>$1.2 μm) and strong absorption coefficient, the peak shifts and distortions are limited.[11] The fundamental reason is that AFM-IR doesn't have direct sensitivity to the real part of the refractive index (n) but depends only indirectly on it, as n affects the local light distribution in the sample.

Table 1 Typical experimental parameters of AFM-IR measurement modalities

AFM-IR method	Laser rep. rate (kHz)	Laser pulse length (ns)	Spectral range	AFM operation	Best spatial resolution (nm)	Typical ΔT (K)
Ring down	1	0.1–500	0.5–16 μm (20 000–625 cm^{-1})[25,31]	Contact	20[31]	1–10
Resonance enhanced	70–1750	10–300	820–1900 cm^{-1} 2700–3700 cm^{-1}	Contact	20[13]	<1
Heterodyne detection	350–1550	10–300	820–1900 cm^{-1} 2700–3600 cm^{-1}	Tapping	10[15]	<1
Peak force	2–8	20	820–1900 cm^{-1}	Peak-force tapping	10[18]	<1

Consequently, for stable measurement conditions, the variability of the spectra is typically limited to small peak shifts and perturbation of the peak ratios related to the physics governing thin film optics rather than intrinsic to AFM-IR.[11] Importantly, the scaling factor ($H_{AFM}H_mH_{th}$) which takes into account the local thermo-mechanical properties of the sample and the local tip–sample mechanical interactions, influences the AFM-IR signal amplitude making quantification of AFM-IR data challenging.[11] However, since the scaling factor is wavelength-independent (*i.e.* constant across a spectrum), spectral ratios are often used as proxy for semi quantitative applications.[23,24]

Since the tip atomistic details are critical for TERS but unimportant for AFM-IR, to obtain a viable AFM-IR signal it is typically not necessary to swap nominally identical tips (a procedure otherwise common in TERS). However, since tip–sample contact dynamics critically determine the AFM-IR intensity (*via* the scaling factor), the selection of AFM-IR measurement parameters (scan speed, set-point, laser power, *etc.*) are very important for obtaining high quality AFM-IR data (constant scaling factor).

2.2 AFM-IR optical configurations

In AFM-IR the sample can be illuminated either from below in total internal reflection (TIR, Fig. 1a) or from above (air side) (Fig. 1b) by means of a parabolic mirror. For TIR,[12] the sample is deposited or fabricated on the top surface of an IR-transparent prism (ZnSe, ZnS, CaF_2). Because of the TIR limited light penetration depth,[11] samples thicknesses are limited to a few μm[21] and preferably less than 1000 nm or 500 nm to ensure a good signal linearity.[11,21] Consequently the TIR configuration may require somewhat complex sample preparations such as microtoming,[25] spin coating,[21] drop casting,[26] or electron-beam lithography.[21,26,27] However, since in TIR there is no propagating light, this configuration avoids direct light absorption in the cantilever and critically limits the background absorption by the environment for measurements in liquids (*i.e.* water).[28–30] This characteristic has also been exploited to extend AFM-IR to the visible range.[31] Hence, in TIR illumination AFM-IR can leverage passive uncoated Si[19,31–34] or SiN[28] cantilevers that don't enhance the field in the proximity of the tip, and can be used, for example, to measure non-perturbatively plasmonic nanostructures.[26,35] This distinctive AFM-IR characteristic contrasts with other near-field techniques such as TERS, scattering-type near-field optical microscopy (s-SNOM) and photo-induced force microscopy (PiFM) which critically depend on and leverage the plasmonic enhancement of the tip. The top illumination (Fig. 1b) simplifies the sample preparation and enables characterization of arbitrarily thick samples, but it requires gold-coated cantilevers to limit self-absorption in the AFM probe. Although the plasmonic enhancement from gold-coated tips is not critical in many AFM-IR experiments,[36] it should be taken into account as a function of the light polarization[37] and it becomes even necessary when measuring the thinnest (*i.e.* monolayer) samples.[13,38–40]

2.3 AFM-IR ring-down measurements

The AFM-IR measurement modality (ring-down) was first introduced by Dazzi using a free-electron laser (CLIO).[12] The development

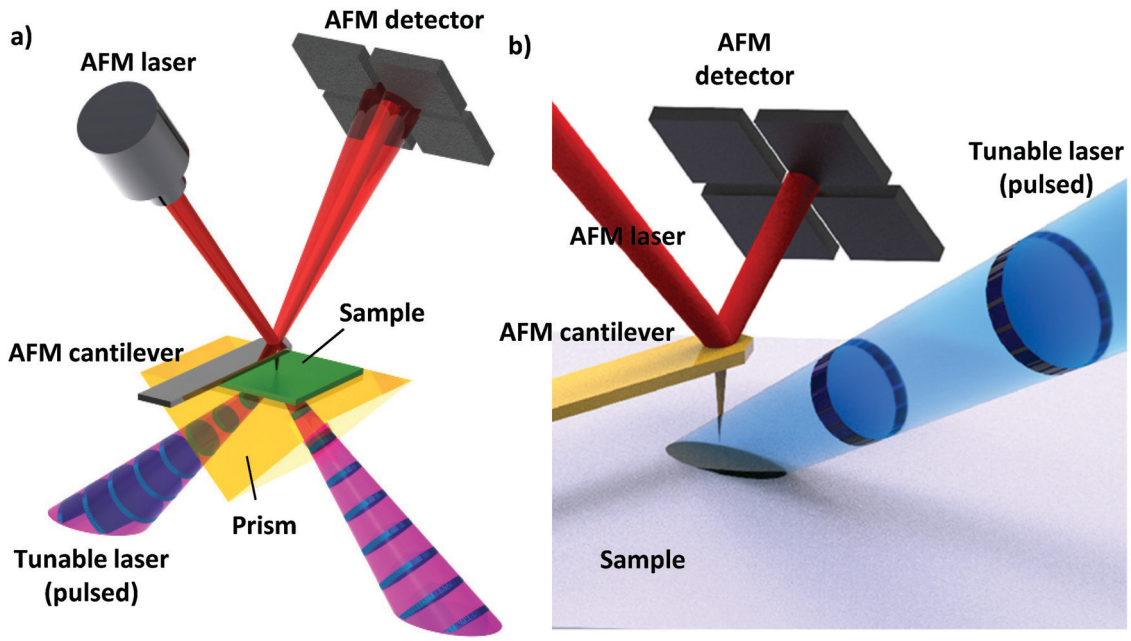

Fig. 1 (a) Schematic of the total internal reflection AFM-IR setup which requires preparing the sample on an optically transparent prism. This configuration minimizes background light absorption in the AFM cantilever and can make use of uncoated AFM cantilevers. Adapted with permission from A. M. Katzenmeyer *et al.*, *Anal. Chem.*, 2013, **85**, 1972–1979. Copyright (2013) American Chemical Society. (b) Schematic of the AFM-IR setup with top-down illumination. This configuration requires the use of a gold coated cantilever to limit light absorption within the cantilever. Adapted with permission from M. Tuteja *et al.*, *Analyst*, 2018, **143**, 3808–3813, The Royal Society of Chemistry.

and availability of tunable table top IR laser sources, such as optical parametric oscillators (OPOs)[25,31] has later enabled the commercialization and fostered the widespread adoption of the technique. These sources are characterized by broad spectral tunability, low repetition rates (typically 1 kHz) and short pulse lengths; (<10 ns).[25,31] As mentioned above, such short pulses, if absorbed by the sample lead to a local increase of temperature (ΔT) proportional to the locally absorbed energy:[10,20]

$$\Delta T(t) = \frac{I_{\mathrm{inc}(\lambda)}}{\rho C_{\mathrm{p}}} R(t)\mathrm{abs}(\lambda) \quad (2)$$

where $R(t)$ is related to the duration of the laser pulse and geometrical parameter of the sample, C_{p} is the heat capacity, ρ is the sample density, I_{inc} the laser incident power and $\mathrm{abs}(\lambda) = \kappa(\lambda)/\lambda$.[34] The ΔT leads to a proportional thermal expansion (u) of the sample according to:

$$u(t) = \alpha K \Delta T(t) \quad (3)$$

where α is the thermal expansion coefficient of the sample and K the factor depending on the size, the geometry and mechanical properties of the sample.[6] The fast thermal expansion causes an impulsive excitation of the cantilever whose response in the time-domain is characterized by the superposition of all the contact resonance modes (hereafter ringdown, Fig. 2a) and can be written as:

$$Z(t,\lambda) = A \sum_n P_n^2 \left(\frac{\sin(2\pi f_n t)}{2\pi f_n} \right) \mathrm{e}^{-\frac{\Gamma t}{2}} \mathrm{abs}(\lambda) \quad (4)$$

which is another way to write the eqn (1), where A contain all of the optical, thermal and mechanical parameters of the sample and the cantilever. P_n correspond the slope of the mode at the apex of the cantilever, f_n is the frequency of the n^{th} mode and Γ is the damping.[6] The Fourier transformation of the ringdown signal reveals the induced contact resonance frequencies of the cantilever (Fig. 2b). Since the AFM-IR mechanical detection scheme works in principle for all wavelengths, its operating range has been recently extended to the near-IR and visible ranges thanks to the availability of wavelength-tunable OPO lasers with suitable characteristics.[31] Because AFM-IR is not limited to the IR range it is also referred to as photothermal induced resonance (PTIR),[5,20,31,41] where "induced resonance" refers to the measurement transduction scheme. Although the term PTIR is more general, the AFM-IR acronym is more commonly used. Therefore, in this work we will use PTIR to refer to experiments in the visible and near-IR ranges and AFM-IR for experiments in the mid-IR.

The photo-thermal expansion contribution to the AFM-IR signal transduction is key for two reasons: first, it provides direct proportionality between the AFM-IR signal and the sample absorption coefficient,[10,11,34] and second, the fast transduction dynamics enable high spatial resolution (down to ≈20 nm in contact-mode[13,31] and ≈10 nm in tapping mode[15,16]). This resolution is much better than the resolution obtained by measuring the sample temperature directly with temperature-sensitive probes, which is instead limited by the heat diffusion in the sample.[42]

The limited sensitivity of conventional cantilevers makes the measurement of thin samples (<50 nm) with the ringdown method, challenging.[21,43] However, the development of picogram-scale nanosized optomechanical AFM cantilevers (Fig. 3a and b) has enabled AFM-IR detection with high temporal resolution (<10 ns) and sensitivity (Fig. 3c and e),[19] thanks to an ultralow detection noise (≈3 fm $\mathrm{Hz}^{-0.5}$) not only on resonance but across wide bandwidth (>25 MHz). These characteristics improve the ringdown signal to noise ratio (50×) and the measurement throughput (2500×) while simultaneously capturing the time-domain thermal expansion dynamics (red trace in Fig. 3c). As discussed in detail by Centrone *et al.*,[19] with these probes the signal (S, black trace in Fig. 3c) is a sum of up to 3 terms:

$$S = S_{\mathrm{osc}} + S_{\mathrm{exp}} + S_{\mathrm{bkg}} \quad (5)$$

where S_{osc} (blue trace in Fig. 3c) describes the cantilever ringdown dynamics, S_{exp} (red trace) describes the probe's motion tracking directly the sample thermal expansion dynamic, and S_{bkg} (green trace) describes the background non-local through-air heating of the probe *via* the thermo-optic effect.[19] S_{osc} is the only measurable signal with conventional cantilevers (see Fig. 2a) or with the optomechanical probes for samples with thermalization dynamics faster than 10 ns, as for a ≈2 nm thick monolayer (Fig. 3e and f). The latter, could be measured with such probes with high signal to noise ratio (≈174) without resonant excitation or plasmonic enhancement. The extraction of the characteristic sample thermalization time (τ_{s}) from S_{exp}, yields the local thermal diffusivity of the sample $D = \eta/(C_{\mathrm{p}}\cdot\rho)$ or, if its heat capacity (C_{p}) and density (ρ) are known, its thermal conductivity (η) according to[19]

$$\tau_{\mathrm{s}} = \frac{4}{\pi^2} \cdot \frac{C_{\mathrm{p}} \cdot \rho \cdot z^2}{\eta} = \frac{4}{\pi^2} \cdot \frac{z^2}{D} \quad (6)$$

where z is the sample thickness (see Fig. 3d). Although these remarkable results from the Centrone's group come at the cost of measurement complexity, they also provide direct experimental evidence of the proportionality between the ringdown amplitude and the magnitude of the initial sample thermal expansion;[19] thus validating the AFM-IR theory developed by Dazzi.[10]

2.4 Resonance-enhanced AFM-IR measurements

The AFM-IR resonance-enhanced mode, introduced by Belkin *et al.*,[13,44] relies on quantum cascade lasers with tunable wavelength and repetition rate (up to a few MHz). The resonant excitation of the cantilever is achieved by matching the laser repetition rate to one of the cantilever contact resonance frequencies (Fig. 2c and d). With this method the sample thermal expansion efficiently excites only one of the cantilever mechanical modes (Fig. 2d) according to:

$$Z(t,\lambda) = A P_n^2 \left(\frac{\sin(2\pi f_n t)}{2\pi f_n} \right) \frac{Q}{2\pi} \mathrm{abs}(\lambda) \quad (7)$$

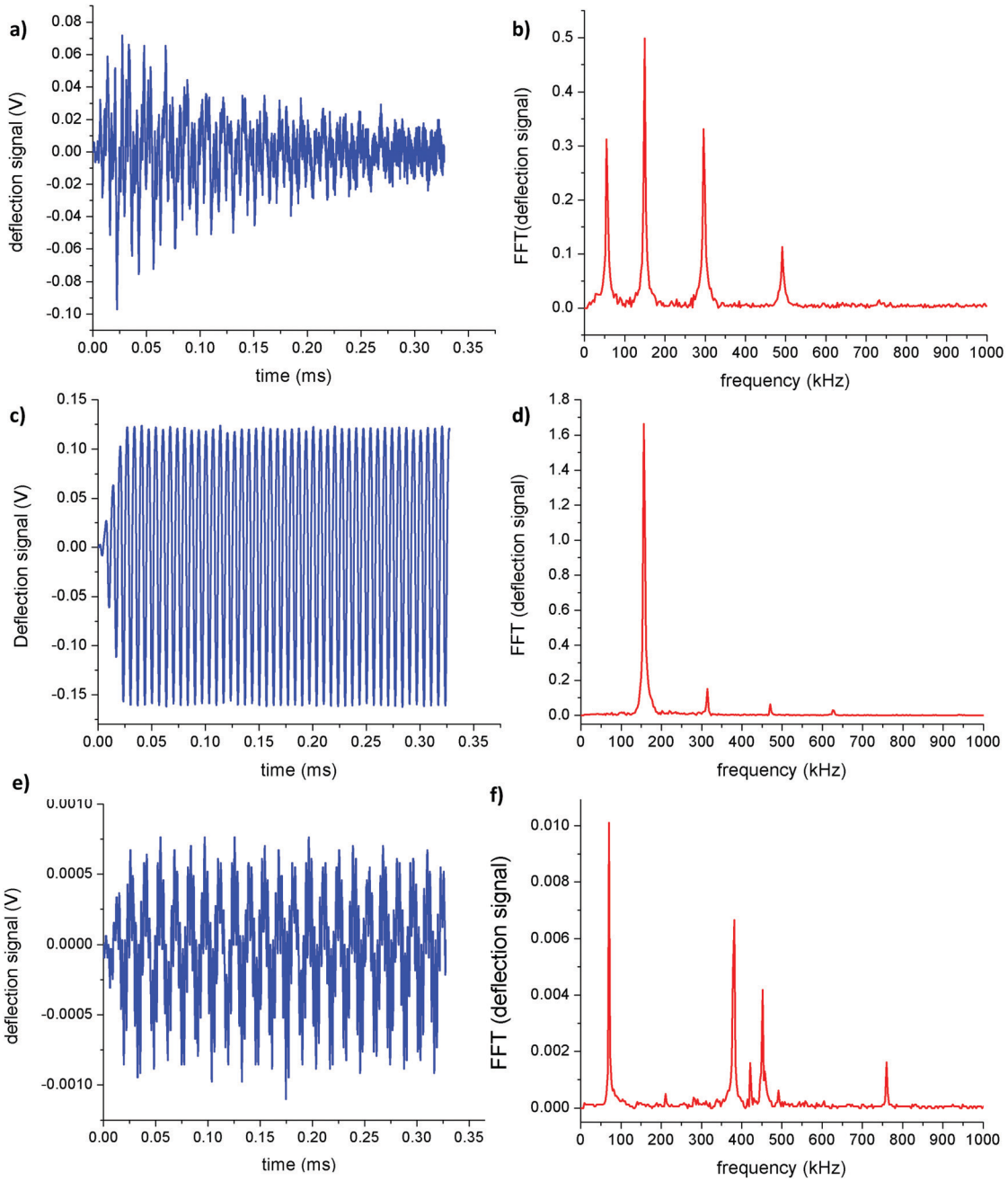

Fig. 2 (a) Typical time domain cantilever ringdown that follows the absorption of short laser pulses in the sample. (b) FFT of the ringdown revealing the first four contact-resonance modes. (c) Typical time domain signal measured by pulsing the laser in resonance (resonance-enhanced mode) with one of the cantilever contact-resonance frequencies (≈160 kHz). (d) FFT of the resonance-enhanced signal showing that the cantilever response mainly consists of the resonantly contact-mode. (e) Typical tapping AFM-IR time-domain signal. (f) FFT of the tapping AFM-IR signal showing the driving tapping-mode frequency at 75 kHz, the laser driving frequency at 375 kHz and the second cantilever mode at 450 kHz at which the signal is demodulated.

where A contains all the optical, thermal and mechanical parameters of the sample and cantilever. P_n correspond to the slope of the mode at the apex of the cantilever, f_n and Q are the frequency and Q-factor of the resonant mode.[6]

Comparing eqn (4) and (7), the amplitude of the only resonantly excited mode is amplified by $Q/2\pi$.[13] This improvement permits detection of samples only a few nanometers thick[45,46] or even monolayers.[13] Because the cantilever resonant frequencies depend on tip–sample contact stiffness (*i.e.* the contact frequency increases with the sample stiffness) AFM-IR experiments can also be used to gather qualitative maps of the sample mechanical properties.[10,47] However, this effect is a drawback for measuring AFM-IR absorption maps, as it locally changes the resonant conditions (*i.e.* the signal amplitude). This challenge can be mitigated by measuring the sample off resonance,[19,48] or by locking the laser repetition rate to the

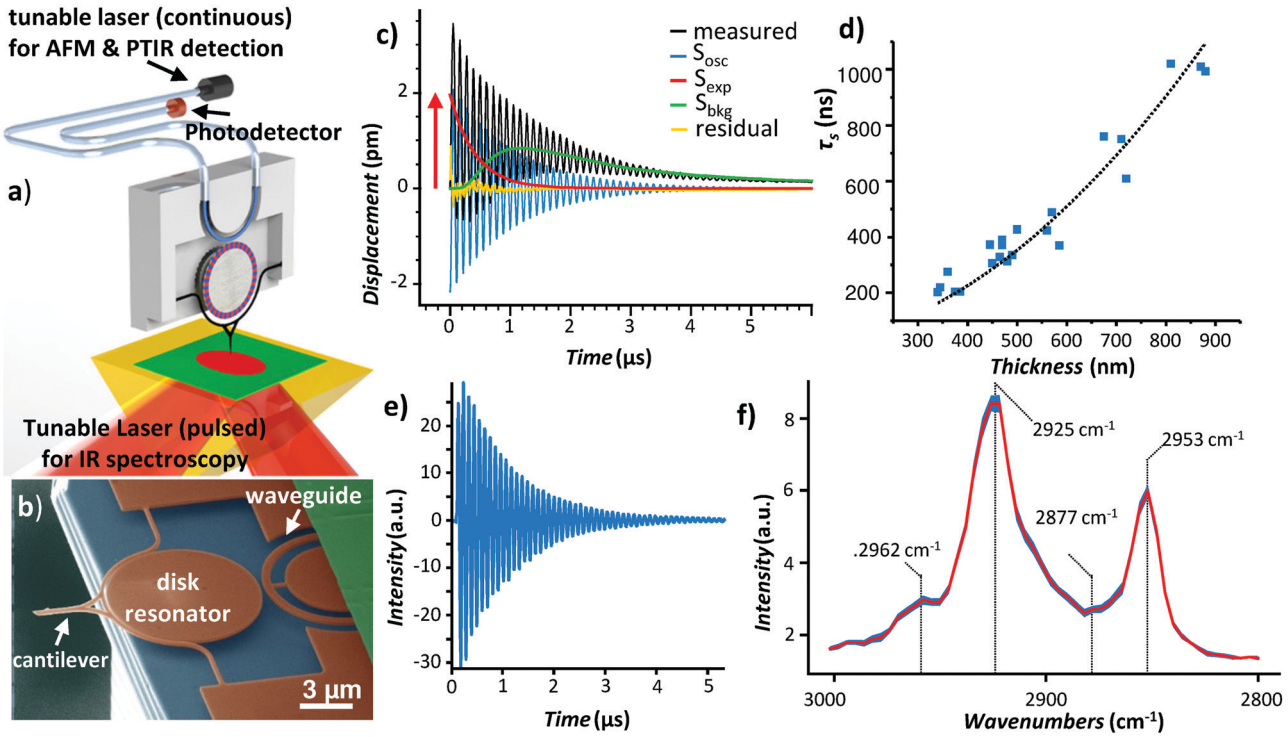

Fig. 3 (a) A fiber coupled tunable CW laser and a photodetector measure the motion of a nanoscale probe of an optomechanical resonator, radically reducing the noise and increasing the measurement bandwidth in AFM-IR experiments. (b) The optomechanical probe consist of a nanoscale cantilever, opto-mechanically near-field coupled to a disk resonator. (c) AFM-IR signal (1388 cm^{-1}, black trace) for 560 nm thick metal–organic framework (HKUST-1) microcrystal. The signal is composed of three contributions as discussed in the text. In addition to the ringdown (blue trace) this setup enables capturing the sample's fast thermalization dynamics (red trace) in AFM-IR experiments. (d) thermalization time as a function of MOF crystal thickness; the black line is given by eqn (6). (e) AFM-IR transducer signal and (f) spectrum of a ≈2 nm thick octadecylchlorosilane monolayer. The red trace and blue shaded-area are the average of 12-spectra from different sample locations and its 95% confidence uncertainty, respectively. Adapted with permission from J. Chae *et al.*, *Nano Lett.*, 2017, **17**, 5587–5594. Copyright (2017) American Chemical Society.

phase of the cantilever resonance in a feedback loop (hereafter phase locked loop, PLL),[15] thereby providing chemical and mechanical stiffness maps simultaneously. However, it should be noted that the PLL can compensate for resonance frequency shifts but not for changes in Q, which are a function of the local mechanical damping properties of the sample.[15] Consequently, with respect to non-resonant ring-down measurement, resonance-enhanced AFM-IR measurements tend to be less stable and the resulting data are more challenging to quantify.

2.5 Tapping-mode AFM-IR measurements

Tapping-mode AFM has been developed to overcome the difficulties for imaging in contact-mode soft or sticky samples, or samples that adhere loosely to the substrate. Not surprisingly samples of such nature are very difficult if not impossible to measure with contact-mode AFM-IR. The recent implementation of AFM-IR in tapping-mode,[14–17] has indeed enabled the characterization of soft,[15,16] stickier,[14] rough[17] or easily displaced samples;[16] further widening the AFM-IR application space.

Tapping AFM-IR also requires lasers with both wavelength and repetition rate tunability and it is based on the heterodyne or multifrequency AFM detection often used in acoustic AFM.[49,50] Tapping-mode AFM-IR enables resonant excitation of the cantilever exploiting the non-linear tip–sample mechanical interactions[51] that enables non-linear mixing of the cantilever oscillation modes response with the laser induced sample expansion. In practice, the cantilever is driven at the first tapping-mode frequency (≈70 kHz in Fig. 2f) and the expansion driven AFM-IR signal is detected at the second tapping-mode frequency (≈450 kHz in Fig. 2f) while the laser repetition rate is set as the difference between the two modes (≈380 kHz in our example). When the above condition is fulfilled, the expression of the expansion driven, second tapping-mode amplitude is given by:[16]

$$\|Z(\lambda)\| = B\chi_s t_{tap}\frac{(f_2 - f_1)}{f_2^2} f_1 Q_2 \mathrm{abs}(\lambda) \quad (8)$$

where B contains the amplitude of the first tapping-mode, the effective mass of the second tapping-mode, the duration of the pulse, and the thermal, mechanical and optical parameters of the sample. χ_s is the non-linear term of elasticity (second order), t_{tap} and f_1 are the time of contact and frequency of the first tapping-mode, f_2 and Q_2 are the frequencies and quality factor of the second tapping-mode. The opposite scheme, tapping at the second mode and demodulating at the first mode is also possible and it is typically carried out with stiffer probes.[17]

Tapping AFM-IR provides a better resolution (≈10 nm)[14–17,46] than contact-mode AFM-IR because the shorter time of contact

t_{tap} limits AFM-IR transduction to the initial thermal expansion and is unaffected by the subsequent spreading of the thermal stress in the sample. However, the non-linear signal transduction typically requires operating the tapped-probe in the strong interaction regime (increased drive amplitude or reduced set-point) and typically using a stronger (2× or more) laser power. Additionally, since in tapping-mode the cantilever resonant frequencies are less affected by the sample mechanical properties, tapping AFM-IR is generally an easier experiment than contact-mode AFM-IR with resonant excitation and PLL feedback.

In another recent work, Wang *et al.* have implemented AFM-IR measurements in peak force mode.[18] The advantage to this approach is the synchronization of the tapping (applied force) to the ringdown measurement leaving the cantilever off the surface the rest of the time leading to high (≈10 nm) spatial resolution and enabling correlative imaging between IR absorption, elasticity and adhesion of the sample. Similar to tapping-mode this method can be applied to measure soft materials.

In summary, the nanoscale spatial resolution coupled with strong similarity between AFM-IR and far-field IR spectra for samples of various thickness (from few nm to micrometer range) are the fundamental aspects that make this technique generally interesting. The key physical mechanism common to all AFM-IR modalities (contact- or tapping-mode) is the transduction of the sample thermal expansion during the contact between the tip and the sample surface. Since its inception, rapid technical advances have enabled improvement of AFM-IR sensitivity,[13,19,46] spectral range,[31] spatial resolution,[15,18] time resolution[19] and lead to an ever growing list of applications (see Section 3) and the possibility to make correlative imaging.[46,52]

3. AFM-IR practical applications

Numerous innovations (see Section 2) have enabled distinct AFM-IR measurement modalities, either in contact-mode, *i.e.* ringdown[12,19,31] and resonance enhanced excitation,[13,45,48] or tapping-mode (heterodyne detection).[15–17] The signal proportionality to the (local) sample absorption coefficient[10,11,21,22] is the most important aspect shared by these methods which enables, to first approximation, direct correlation between AFM-IR and far-field IR spectra.[22] Therefore, AFM-IR translates to the nanoscale many of the benefits of IR analysis, such as: identification of materials,[17,22,53] functional groups,[39,54] molecular conformations,[28,55] crystals' polymorphic forms[56,57] (or amorphous state), isotopic labelling,[14,58,59] and multivariate analysis.[60] Beyond vibrational (IR) spectroscopy, AFM-IR permits nanoscale optical investigations of optical modes (*i.e.* plasmons[26,27,61,62] and polaritons[63,64]) and, thanks to the extension to the near-infrared and visible ranges,[31] nanoscale characterization of bandgap,[41,65,66] and defects.[65] Additionally, AFM-IR measurements (in ringdown mode) can also provide qualitative information on the sample nanoscale mechanical properties.[23,47] and even quantitative information on the sample local thermal conductivity[19] when using novel nanoscale optomechanical AFM probes.[19] Finally, the recent implementation of AFM-IR in liquids[28,29] also holds great promise for new applications in biology and medicine.

Since its first demonstration,[12] the list of AFM-IR applications has expanded steadily, including polymer science,[22,56–58,67] photovoltaics,[41,65,66,68] plasmonics,[26,27,61,69,70] chemistry,[54,71] corrosion science,[59] 2D materials,[39,54,63,64,72] pharmaceuticals,[73] drug delivery,[14–16] medicine,[28,55,60] biology,[30,45,60,74] phytology,[75] geology[76–78] and art conservation.[17,79] Because of the escalating number of AFM-IR/PTIR publications (≈3-fold more in the 2016–2018 period than in the whole preceding decade) and because of former reviews,[5,6,34,37,80] here we discuss several representative, recent examples, rather than providing an omni-comprehensive list. The examples encompass the different AFM-IR measurement modalities introduced in Section 2.

3.1 Recent AFM-IR applications in polymer science

AFM-IR applications is polymer science[14,22,56–59,67,81] are abundant because polymers require understanding and control over their many compositional and structural degrees of freedom at the nanoscale, and because their properties (strong IR absorption, large α, and small η) are ideal for AFM-IR signal transduction.[10,11,25]

For example, AFM-IR was used recently to characterize the intricate chemical distribution in spherulites composed of poly(3-hydroxybutyrate) (PHB) and poly(ethylene glycol) blends as a function of the crystallization conditions.[81] In another example at an even smaller scale (≈40 nm), AFM-IR was used for peering into chemical composition details of epoxy resins; cross-linked polymers that, to a first approximation, are often considered chemically homogeneous. Contrary to these assumptions, Morsch *et al.* showed that the nanoscale chemical heterogeneity (*i.e.* variable cross-linking density) in epoxy networks[67] is responsible for heterogeneous water uptake.[59] Understanding the long-term evolution and stability of these hydrophilic regions is crucial for engineering epoxy coating in corrosion applications.[59]

In another elegant example, Rickard *et al.*[58] used a deuterium-labelled polymer to understand the chemical distribution of an experimental three-component blend made by polyethylene (PE), polypropylene (PP) and deuterated polyethylene–propylene copolymer (d-PEP). Plastic waste streams often contain both PE and PP which, however, are immiscible and need to be separated or require the addition of a compatibilizing polymer (d-PEP in this case) to yield a material with suitable properties when recycled together. The deuteration of the d-PEP phase was necessary in this case to spectroscopically distinguish the PEP copolymer phase within the blend (64/27/9, PE/PP/d-PEP mass ratio). The results (Fig. 4) clearly show that the d-PEP copolymer is dispersed in the PE matrix but doesn't mix with the PP phase,[58] suggesting that, for best performance, further engineering of the compatibilizing polymer may be necessary for partitioning it at the PE and PP interface. A similar strategy (deuteration of the lipid phase) was used by Tuteja *et al.*[14] to map the distribution of a three-component blend consisting of a lipid–polymer hybrid film loaded with

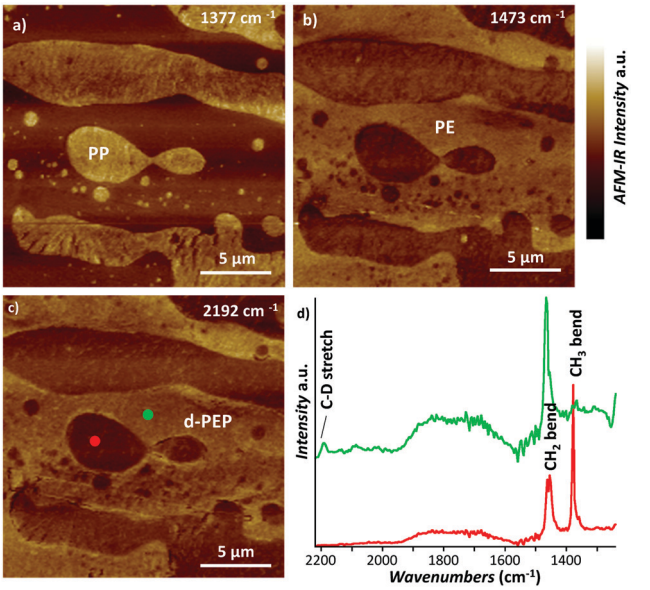

Fig. 4 AFM-IR images of a three-component blend made by polyethylene (PE), polypropylene (PP) and deuterated polyethylene–propylene copolymer (d-PEP) obtained at (a) 1377 cm^{-1} (CH_3 bending of PP), (b) 1473 cm^{-1} (CH_2 bending of PE) and (c) 2192 cm^{-1} (CD_2 stretching of d-PEP). (d) AFM-IR spectra obtained at the color-coded locations marked in panel-d. The data show that the d-PEP copolymer partitions in the PE phase but does not mix with the PP phase.[58] These AFM-IR experiments were obtained in ringdown mode. This figure has bene adapted from M. A. Rickard (ref. 58) with permission from Elsevier, copyright 2020.[58]

paclitaxel, a chemotherapeutic drug. In this case, AFM-IR images revealed enhanced partitioning of paclitaxel at the lipid–polymer phase boundaries which explain the enhanced and synergistic drug-release of the hybrid film, compared to polymer only or lipid only films.[14]

AFM-IR was also used to identify at the nanoscale the polymorphic forms of crystalline polymers[57] and to determine the fraction of crystalline *vs.* amorphous material[56] in polymer samples. For example, Gong and coworkers observed a heterogeneous distribution of polymorphs with a core–shell structure even in a single poly[(*R*)-3-hydroxybutyrate-*co*-(*R*)-3-hydroxyhexanoate] (PHBHx) electro-spun fiber.[57] Specifically, the thermodynamically-stable α-form (characteristic absorption at ($\approx$1728 cm^{-1}) comprised the fiber core, while the metastable β-form ($\approx$1740 cm^{-1}) was found in a thin ($\approx$10 nm thick) outer shell, regardless of the fiber size.[57] Crystallization of the metastable β-form occurs due to the extremely rapid solvent evaporation in the outer portion of the fiber in the electrospinning process. Similarly, Rebois *et al.*, used AFM-IR to determine the crystalline ($\approx$15%) and amorphous ($\approx$85%) fractions of PHB inside bacteria which produce and store PHB within intracellular vesicles. Such results reveal that the small vesicles kinetically restrain PHB crystallization with respect to commercial PHB ($\approx$57% crystallinity), a characteristic that enhance the bioavailability PHB to the bacteria. Interestingly PHB crystallinity within the vesicles could be increased up to $\approx$68% (*i.e.* beyond commercial grade) by exposing the bacteria to chloroform vapors.[56]

3.2 AFM-IR characterization of metal–organic frameworks

The synthesis of metal–organic frameworks (MOFs),[71,82] has also benefitted from AFM-IR chemical specificity. MOFs[82] are nanoporous materials consisting of inorganic ions bridged by organic linkers. Like child's building blocks, MOFs have stimulated chemists' imagination leading to the assembly of chemically diverse structures with tailored properties for separation, catalysis, drug delivery, and other applications.[82] For example, AFM-IR was used to determine the distribution of linkers in MOF single microcrystals composed of two functional linkers,[54] and to understand the growth mechanism of MOF thin films;[71] a knowledge that has enabled growing films of better quality and at a $\approx$20-fold faster rate. Finally, the thermal conductivity of MOF single microcrystals, not measurable with other techniques, was measured in AFM-IR experiments using new nanoscale optomechanical AFM probes capable of capturing the sample thermal-expansion dynamic with $\approx$10 ns time-resolution.[19]

3.3 AFM-IR extension to the visible range and its applications to photovoltaics

Since the AFM-IR method extends beyond the IR range, it is also often referred to as photothermal induced resonance (PTIR) technique. PTIR in the near-IR and visible ranges,[31] enables measuring optical properties (*i.e.* bandgap[41,66,68] and defects)[65] and chemical composition with a wavelength-independent resolution, which is useful in optoelectronic applications.[41,65,66,68,83] Contrary to other AFM-based, primarily near-surface sensitive, techniques such as s-SNOM,[5] PTIR has the ability probe the whole device thickness[11,21] (typically $\approx$500 nm for PV devices).

Historically, the efficiency of photovoltaic technologies has improved very slowly despite great efforts.[84] In contrast, the efficiency of the recently developed organic–inorganic perovskite solar cells skyrocketed well above 20%, despite fabrication with cheap, and potentially high-throughput, solution processes. However, the understanding of perovskite fundamental properties has generally trailed the pace of their efficiency improvement and PTIR has been instrumental for closing some of these knowledge gaps. For example, it has provided the first direct evidence of ion migration[68] in these materials and has verified their ferro-elastic nature;[66] two properties related to the photovoltaic hysteresis[85] of unstable perovskite devices.

Another debated aspect is whether the improved stability and carrier diffusion length of mixed chloride/iodide perovskite solar cells ($CH_3NH_3PbI_{3-x}Cl_x$)[41] are provided by incorporation of Cl^- in the film (of difficult detection at low concentrations) or just by Cl^- mediated crystallization of a non-chlorinated perovskite. The lack of suitable laser sources impedes PTIR measurements of Pb–Cl vibrations, However, since incorporation of Cl^- in the perovskite structure widens the bandgap,[86] the bandgap derived from nanoscale absorption spectra (Fig. 5) was used as a proxy of the local chloride content in PTIR experiments in the visible range.[41] Image ratios are convenient to display absorption information that is independent from

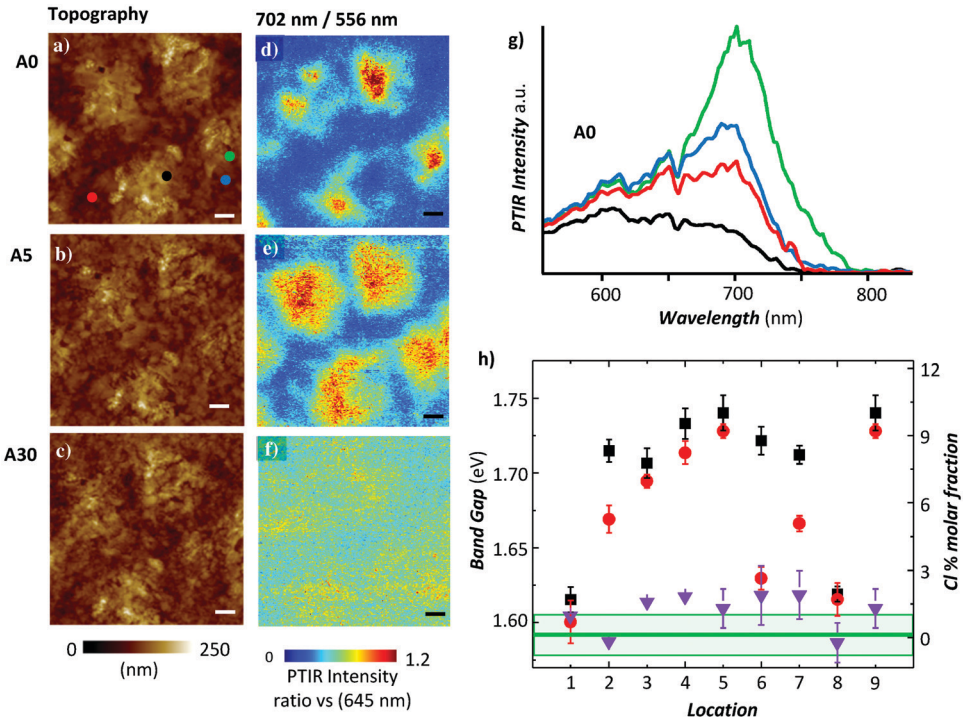

Fig. 5 $CH_3NH_3PbI_{3-x}Cl_x$ perovskite AFM topography maps (a–c) and corresponding absorption ratio (702 nm/556 nm, *i.e.* 1.77 eV/2.23 eV) maps (d–f) as a function of annealing: A0, as prepared (a and d), A5, 5 min annealing at 95 °C (b and e), A30, additional annealing for 5 min at 95 °C and for 20 min and at 110 °C (c and f). The red and blue tones indicate Cl-poor and Cl-rich regions, respectively. All scale bars are 1.0 μm. (g) PTIR spectra obtained at the color-coded locations in panel-a for the as prepared sample. (h) Local bandgap (left axis) and local Cl% content (right axis) obtained by linearly fitting the spectra at 9 locations as a function of annealing: as prepared sample (A0, black squares), A5 (red circles), A30 (purple triangles). Upon annealing the local bandgap and Cl^- content decreases at all locations, approaching the bandgap of the $CH_3NH_3PbI_3$ phase (green horizontal line). The light green rectangle and error bars represent a single standard deviation in the calculation of the local bandgap due to the linear fitting of nanoscale the absorption spectra.[41] These AFM-IR experiments were obtained in ringdown mode. Adapted with permission from J. Chae *et al.*, *Nano Lett.*, 2015, **15**, 8114–8121. Copyright (2015) American Chemical Society.

topographic details. The absorption ratio maps and spectra in Fig. 5 show strong bandgap heterogeneity in the as prepared sample, which progressively decreases with annealing approaching the bandgap of the pure $CH_3NH_3PbI_3$ phase in the fully annealed film. Notably, despite the small Cl^- content ($<2.0\%$ mol mol^{-1}) $CH_3NH_3PbI_{3-x}Cl_x$ films display much better stability than morphologically similar $CH_3NH_3PbI_3$.[41] A similar investigation from the same group has revealed heterogeneities of the bandgap and of the distribution of shallow and deep defects in CdTe commercial solar cells.[65] A recent review on the application of IR nano-spectroscopy techniques for the characterization of energy related materials is available elsewhere.[87]

3.4 AFM-IR applications in nano-optics

As discussed in previous reviews.[5,6,37] AFM-IR spurred several nano-optics applications. Briefly, the Centrone's group used AFM-IR to image dark plasmonic modes[26,27] and to quantify with nanoscale resolution the surface-enhanced infrared absorption (SEIRA)[27,35,69,70] in proximity of plasmonic resonators of various shapes.[69] The thermo-plasmonic and SEIRA effects were also studied recently by Mancini *et al.*, in vertical antennas, highlighting the two major near-field characteristics of surface plasmons: field-confinement and nanoscale heating.[88] AFM-IR has also revealed the nanoscale origin of circular dichroism in plasmonic antennas, which is related to nanoscale differences in the Ohmic loss (*i.e.* localized heating) induced by circularly polarized light of opposite directions.[61] In a different work, the strong p-light polarization induced near-field under the AFM tip was used to measure the epsilon-near-zero mode, *i.e.* when the real part of the refractive index approaches 0 in a thin ($\approx$2 nm) SiO_2 film.[40]

Plasmons attract attention because, of the strong near-fields and because their resonant wavelength can be engineered across a wide spectral range.[89] The ohmic dissipation of plasmons can be useful in the photothermal treatment of cancer,[90] but more typically the high losses and short life time (few fs) of plasmons in metals hinder their applications.[89,91] In contrast, phonon polaritons, collective excitations in polar dielectrics, have longer lifetimes (few ps) and lower losses[91] but exist only within the Restrahlen band (*i.e.* in the spectral region between the longitudinal and the transverse optical phonons).[91] The crystal anisotropy of hexagonal boron nitride (hBN), one of the many 2D-materials, confers hyperbolicity to its phonon polaritons, *i.e.* the ability to propagate with arbitrarily large wave vectors, thereby enabling optical confinement to very small volumes. Indeed, theoretical calculations[63,92] on hBN frustum (truncated cone) nanostructures have predicted

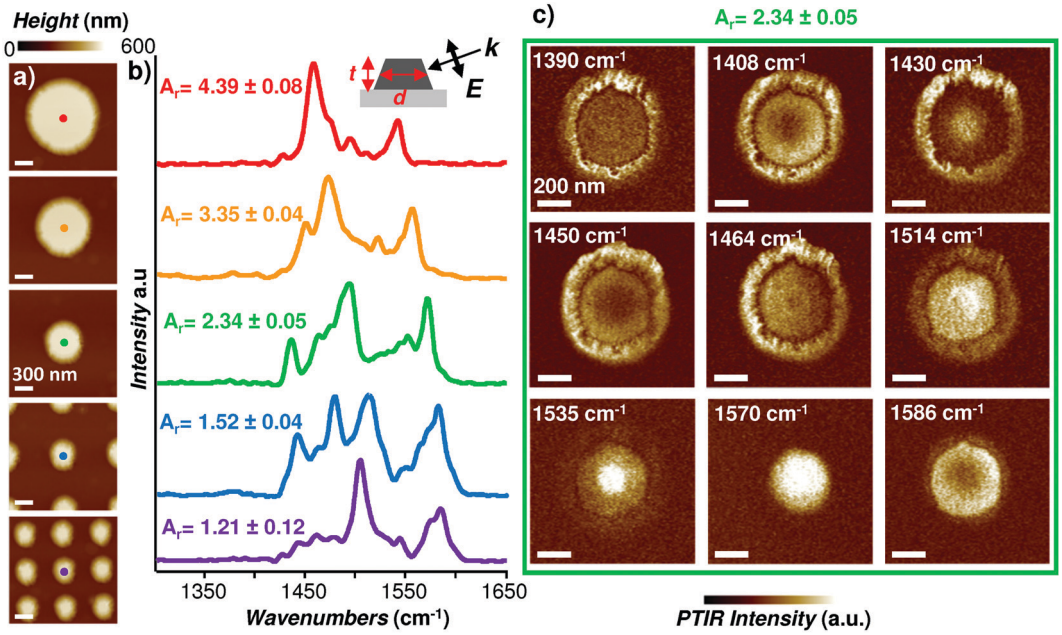

Fig. 6 (a) AFM topography of five representative hexagonal boron-nitride (hBN) frustums with different aspect ratio ($A_r = d/t$). All the frustums have a height of 256 nm ± 4 nm. Scale bars 300 nm. (b) AFM-IR absorption spectra (p-polarization) obtained by positioning the AFM tip at the center of representative frustums, as indicated in panel-a. The schematic of the incident polarization used for the measurements, along with the depiction of the quantities t and d, are provided as an inset. (c) AFM-IR maps (scale bars 200 nm) at selected wavelengths highlighting near-field patterns of the hBN polaritons for the A_r = 2.34 frustum.[63] These AFM-IR experiments were obtained in ringdown mode. Adapted with permission from L. V. Brown, *Nano Lett.*, 2018, **18**, 1628–1636. Copyright (2018) American Chemical Society. The AFM-IR images at 1408 cm^{-1} and 1464 cm^{-1} are from the same dataset reported by Brown *et al.* but have not been published previously.

the existence of several volume-confined polaritonic modes, characterized by 3 discrete modal indexes (*i.e.* quantum numbers), but only a subset of these predicted modes could be observed with s-SNOM.[93] In contrast, AFM-IR mechanical transduction is independent from the mode radiation efficiency to the far-field, and has enabled measuring many of the theoretically predicted modes,[63] see Fig. 6. Phonon-polaritons in hBN flakes as thin as 4 nm have been measured exploiting the plasmonic enhancement between a gold tip and gold substrate.[64]

3.5 AFM-IR characterization of 2D materials

Beyond nano-optics, 2D materials[94] such as hBN, graphene, WSe, *etc.* attract great interest in electronics, optoelectronics, and many other applications. Remarkably, the properties of these materials can be modified either by covalently binding functional groups, by absorbing small molecules, or by stacking multiple 2D materials layers to form synthetic heterostructures. The need to characterize the nanoscale distribution of functional groups[39] and molecules[72] intentionally added or of spurious contaminants[53] that screen the material intrinsic properties, has incited recent AFM-IR applications. For example, Bartlam *et al.* measured the distribution of sulfonated pyrenes adsorbed on the surface of a reduced graphene oxide single layers (1.7 nm thick sample).[72] Liu *et al.*, characterized the complex distribution of oxygen bonds in graphene oxide (GO), showing a relatively higher concentration of C–O bonds on the GO plane and a relatively higher concentration of C═O bonds at the GO flake edges.[39] Both works achieved monolayer sensitivity with the conventional AFM-IR ring-down mode exploiting the near-field enhancement between the gold-coated tip and gold-coated substrate. Schwartz *et al.* used resonance enhanced AFM-IR to identify the composition of nanoscale contaminants[53] (down to ≈1.8 amol) trapped in heterostructures composed of pairs of WSe2, WS2, and hBN layers which trapped polydimethylsiloxane (PDMS) and polycarbonate residue, corresponding to the stamp materials used for their fabrication. This knowledge spurred a new stamp cleaning procedure that eliminated or reduced the contaminants below detectable amounts.[53]

3.6 Recent AFM-IR chemical imaging applications in the life sciences

AFM-IR applications in the life sciences are also widespread, fostered by the generally large expansion coefficient of biological samples. However, these materials are characterized by a broad range of mechanical properties; and, since very soft samples make the AFM-IR signal transduction inefficient,[11,15] earlier studies in contact-mode were carried out on somewhat stiffer samples.[95] The recent introduction of tapping-mode AFM-IR,[14–16] has enabled measuring samples that are softer,[15,16] stickier,[14] rougher[17] or easily displaced by the AFM-tip.[16]

As previously reviewed in detail,[6] the Dazzi's group used AFM-IR to study the production of biofuels in bacteria,[33,96] yeasts and microalgae.[6] Critical to this application, is the AFM-IR ability to measure nanoscale absorption for samples

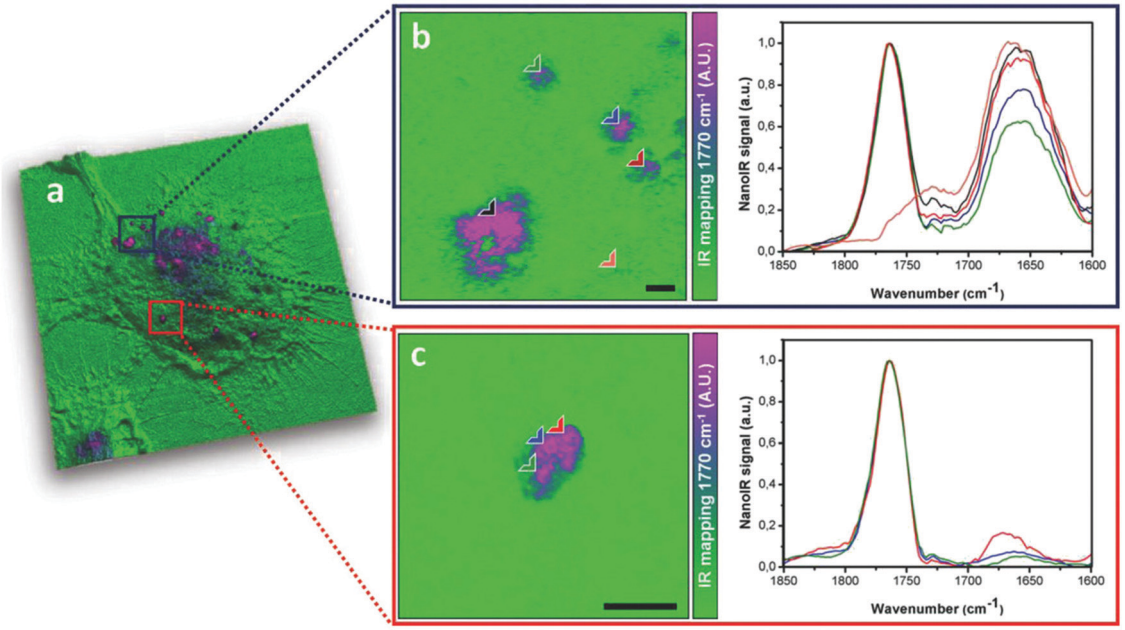

Fig. 7 3D overlay image of IR absorption at 1770 cm^{-1}, characteristic of polylactic acid, inside a macrophage cell. (b and c) AFM-IR maps (1710 cm^{-1}) and spectra (at color-coded marked locations) of the two areas highlighted in panel (a) containing polylactic acid nanoparticles. The scale bar represents 500 nm.[52] These AFM-IR experiments were obtained in resonance-enhanced mode. This figure has bene adapted from E. Pancani (ref. 52) with permission from The Royal Society of Chemistry, copyright 2020.

with thicknesses even in excess of 1 μm,[21] which was harnessed to map the distribution of biofuel-containing vesicles,[33] viruses,[95] nanoparticles,[52,97] subcellular structures[98] and proteins[38] inside single organisms and cells. For example, the distribution of drug delivering nanoparticles (as small as ≈170 nm) made with polylactic acid inside macrophages,[52] was revealed leveraging the particles' intrinsic vibrational signatures (Fig. 7), in place of the commonly employed fluorescent tags that may modify the particles' biological fate. Recently the Wood's group reported the first AFM-IR multivariate analysis applications.[60] Red blood cells infected with malaria parasites (*Plasmodium falciparum*) were characterized at different stage of infection, revealing subcellular structures, suggesting that AFM-IR studies of antimalarial–drug interactions with the parasite may become possible.[60] In this case, AFM-IR images at discrete wavenumbers, corresponding to large variances in survey spectra, were corrected for drift before hierarchical cluster analysis, which revealed regions of the cells rich in lipids, DNA, hemoglobin or hemozoin, the byproduct of parasite-induced hemoglobin degradation.[60] The same group, used principal component analysis (PCA) of AFM-IR spectra to discriminate between Gram-positive and Gram-negative bacteria based on their cell wall spectral characteristics, see Fig. 8.[60] This is not entirely surprising since, in first approximation, Gram-negative bacteria have a thin cell wall consisting of an inner and outer membrane sandwiching a thin peptidoglycan layer. In contrast, Gram-positive bacteria have a thick cell wall consisting of an inner membrane and a thick layer composed by peptidoglycan and teichoic acid. In the same work, the authors also observed the formation of a cell wall septum (≈45 nm thick) in a living bacterium prior to the cell division (Fig. 8). Although the data acquisition (ringdown) in these studies was slow,[60,99] the recent development or rapidly tuning lasers enabling fast (≈1 s) AFM-IR spectral acquisition,[15] suggest that AFM-IR multivariate analysis may become more common place in the near-future.

The recent introduction of tapping-mode AFM-IR has enabled the characterization of several nanostructured drug delivery media such as lipid–polymer hybrid films,[14] liposomes[15] and core–shell polymeric nanoparticles,[16] which are difficult to measure in contact-mode due to their unfavorable mechanical properties.[15] These advanced formulations attract interest because they deliver therapeutic cargos overcoming the conventional tradeoff between therapy efficacy and the side effects. For example, liposomes nanocarriers increase therapy efficacy while minimizing side-effects by delivering difficult to administer therapeutics with better selectivity and efficiency. Tapping-mode AFM-IR has enabled label-free detection and mapping of the distribution of ≈1000 cytarabine molecules (≈1.7 zmol), a chemotherapeutic drug, inside single liposomes[15] (≈80 nm diameter). This characterization enables classification of empty and drug-loaded liposomes, which is necessary for determining the drug encapsulation efficiency and the effective dosage. Similarly, tapping-mode AFM-IR was used to establish that another drug, pipemidic acid (only 1% weight fraction), is loaded on the external surface of core–shell polymeric nanoparticles; a formulation useful for burst drug release.[16]

3.7 AFM-IR conformational analysis and measurements in water

Because attainment of proteins native structure by folding, is key to life-enabling biological processes and, conversely, protein misfolding can generate toxic aggregates that are related

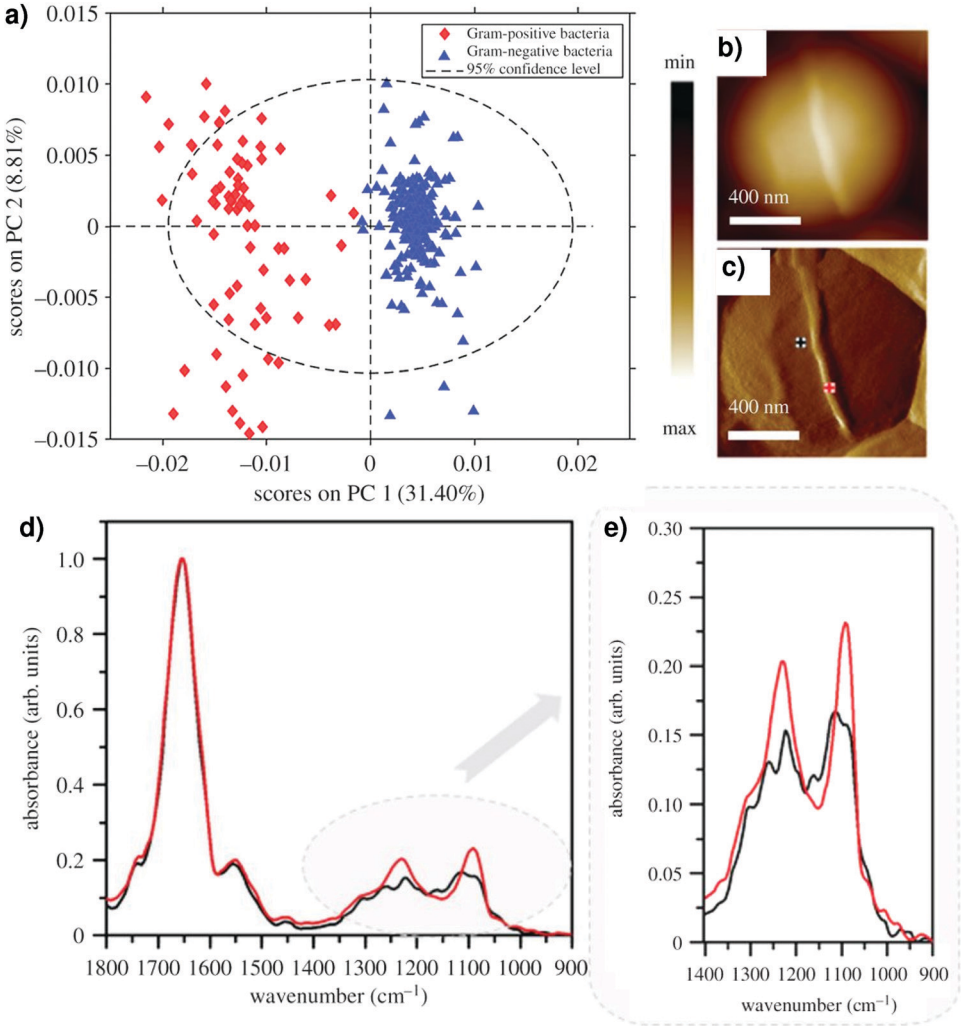

Fig. 8 (a) PCA scores plot (PC1 *versus* PC2) for the second derivative of AFM-IR spectra dataset (n = 327) obtained from six different bacteria in the 1400 cm^{-1} to 950 cm^{-1} spectral range. The plot shows separation of Gram-positive bacteria (red markers) and Gram-negative bacteria (blue markers) along PC1, which captured 32% of the spectral variance. (b) AFM height and (c) AFM deflection image of a *Staphylococcus aureus* dividing cell obtained before recording AFM-IR spectra (d and e) at the color-coded marked positions; *i.e.* on the forming septum (red) and non-septum (black). The spectra, normalized to amide I band, show stronger intensity on the septum for the bands associated with carbohydrate and phosphodiester groups of cell-wall components.[60] These AFM-IR experiments were obtained in ringdown mode. This figure has been adapted from ref. 63 with permission from The Royal Society of Chemistry, copyright 2020.

to >50 human diseases,[100] determination of proteins' folding patterns is an important IR spectroscopy application.[101] This typically requires deconvolution of the amide I band (≈1650 cm^{-1}) to reveal the proteins' secondary structure, based on the common bonding patterns (*i.e.* conformations) of the protein backbone, such as α-helix, random coil, α-turn, β-sheet, β-turn, *etc.*[101] Since Ruggeri *et al.* pioneering work[55] on the aggregation pathways of the Josephin domain of ataxin-3, responsible for type-3 spinocerebellar ataxia, an inheritable protein-misfolding disease, AFM-IR was used to characterize molecular conformations in a wide spectrum of applications.[28,45,46,102–105] For example, Paluszkiewicz *et al.* showed that the progress of cataract disease in human eye lens is spatially heterogeneous and it is correlated to the local secondary structure of proteins (β-turn/parallel β-sheet for the normal tissue *vs.* anti-parallel β-sheet for the diseased tissue).[103] Giliberti *et al.* leveraged conformational changes of transmembrane proteins detected with AFM-IR to reveal heterogeneity of the proteins hydration states at the nanoscale.[45] Very recently, the same group introduced difference AFM-IR spectroscopy to study the (visible) light induced conformation changes in photosensitive transmembrane proteins.[106] Other examples include studies of: fibrillar aggregates of the first exon of Huntington protein (Exon1),[102] electron-induced conformational transitions in silk-proteins based electron-beam resist,[104] and to assess the toxicity of nanodiamonds inside cells.[97]

Such broad application range is not surprising since protein aggregates often show conformational heterogeneity at the nanoscale due to complex equilibria that depend on the proteins sequence and on environmental interactions.[100] Many protein misfolding diseases arise when the control systems that keep the proteins in their soluble state loose efficiency

(common with aging) or because pathological mutations increase the propensity of protein aggregation.[100] In Alzheimer's disease, for example, stronger and stronger evidence suggests that small fibrillar species, referred to as oligomers, are the most toxic species.[100] The environmental influence on the proteins' conformation, and the need to characterize cells under native conditions, are strong drivers for AFM-IR experiments in water.[28] However, AFM-IR measurements in water are challenging because of water's IR absorption background and because the increased drag in water dampens the cantilever oscillations at the core of the AFM-IR signal.[28,30] The first AFM-IR experiment in water[30] (ring-down method) was made possible by ATR illumination and by a 2 μm thick sample (*Candida albicans* fungi) which minimized the water absorption background, but resulted in a low (≈3.3) signal-to-noise ratio (SNR) due to fluid drag. This experiment remained an isolated attempt until Belkin *et al.* succeeded in measuring a 20 nm thick PMMA sample in water, 9 years later.[29] To measure such a thin sample in liquid, the authors resorted to an array of provisions to increase the signal and to reduce the water background: (i) resonance-enhanced excitation (ii) deuterated water and (iii) the tip-enhancement between a gold-coated probe and a germanium prism which, however, also resulted in a low (≈5) SNR.[29] More recently, the Centrone's group showed that for thicker samples (≈200 nm) it is possible to obtain AFM-IR spectra in air and water with comparable SNR and spatial resolution.[28] More importantly, the high (>70) SNR achieved in water was sufficient to enable nanoscale conformational analysis of supramolecular aggregates made by diphenylalanine (FF), the core recognition module of Alzheimer's β-amyloid peptide, and its *tert*-butoxycarbonyl (Boc) derivative, Boc-FF (see Fig. 9).[28] Even though the two peptides differ just by one chemical group, the amide-I band in AFM-IR spectra reveal that the conformation of their fibrillar aggregates in water is different at the single fibril level (Fig. 9). These measurements suggest that ATR illumination and resonance-enhanced excitation are key for AFM-IR measurements in water, despite the lower cantilever *Q*-factors in liquid.

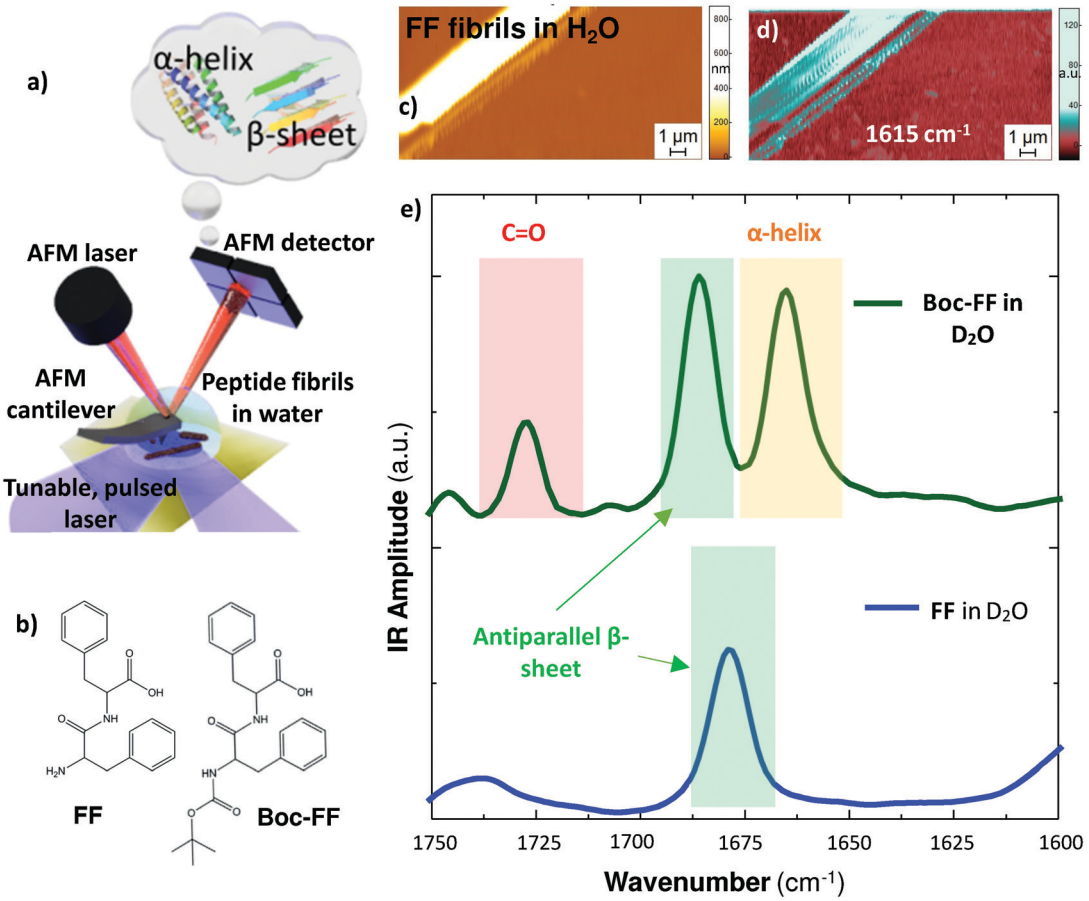

Fig. 9 (a) Schematic of the AFM-IR measurement in water which require illuminating the sample from below in total internal reflection to minimize the water absorption background. (b) Chemical structures of diphenylalanine (FF) and *tert*-butoxycarbonyl of diphenylalanine (Boc-FF) peptides. (c) AFM topography (*i.e.* morphology) map and (d) IR absorption map (1615 cm^{-1}) for FF fibrils in H_2O. (e) Comparison of the average AFM-IR spectra obtained on FF (bottom) and Boc-FF (top) fibrils in the amide I (green and yellow) and C=O stretching (red) spectral ranges. Although the two peptides differ just by one chemical group, their conformation in water (either D_2O or H_2O) is different at the single fibril level.[28] These AFM-IR experiments were obtained in resonance-enhanced mode. Adapted with permission from G. Ramer *et al.*, *ACS Nano*, 2018, **12**, 6612–6619. Copyright (2018) American Chemical Society.

The tip enhancement, is necessary for thinner (<200 nm) samples and the use of deuterated water is useful to avoid spectral overlap but is less critical. AFM-IR measurements in water could also potentially benefit from novel high-sensitivity nanoscale opto-mechanical AFM probes, developed by the Centrone's group, due to the predictably lower fluid drag of the nano-sized cantilever.[19]

3.8 AFM-IR applications in geology

While several techniques are available to study the composition of inorganic minerals in rocks at the nanoscale, those typically are ineffective for determining the composition of organic inclusions. AFM-IR has recently closed this gap enabling characterizing of organic inclusions in rocks[76,77] and meteorites.[46,107] For example Yang *et al.* assessed the heterogeneity of organic macerates at different level of maturity in shale,[76] a sedimentary rock composed by organic matter dispersed in a mineral framework, and responsible for the recent oil extraction boom in the United States. The data show that with increasing shale maturity, the composition of the organic phases evolve and get progressively enriched with aromatic carbon and depleted of oxygen and aliphatic carbon.[76] AFM-IR was even used to characterize carbon inclusions in 3.7 billion years old rocks of possible biogenetic origin.[77] Similarly, organic inclusions in two widely studied meteorites (carbonaceous chondrites)[107] and in Antarctica's micrometeorites[46] revealed strong chemical heterogeneity at the nanoscale. For example, Fig. 10 shows that in an Antarctica's micrometeorite the ratio map of C=O absorption (carbonyl, 1710 cm^{-1}) and C=C absorption (1600 cm^{-1}) is highly heterogeneous.[46] In another earth science application, AFM-IR was used to characterize the composition of atmospheric aerosol particles, which also typically consist of complex nanosized chemical mixtures.[78]

3.9 AFM-IR applications in art conservation

Finally, art conservation is another field where samples are often composed of complex chemical mixtures of organic and inorganic compounds and can benefit from AFM-IR characterization.[79,108] While the chemical composition in works of art can vary greatly, many degradation processes challenging their conservation are of common occurrence, but often not well understood. For example, Latour *et al.* leveraged AFM-IR to study the degradation of historic parchment obtained from animal skin. Parchment mainly consists of collagen that can denaturalize and lead to the formation of gelatin; a process that can be followed at the nanoscale

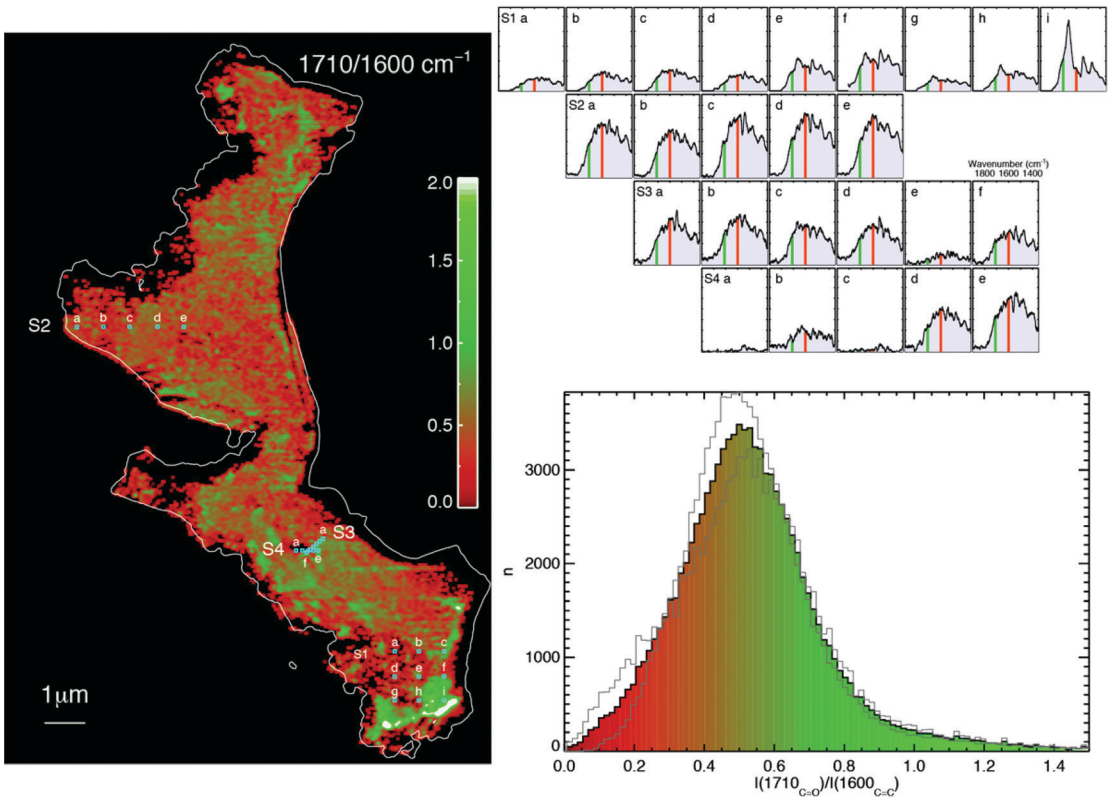

Fig. 10 Left: AFM-IR image ratio obtained by dividing the intensity at 1710 cm^{-1} (C=O) with respect to the intensity at 1600 cm^{-1} (C=C) for the DC16-14-309-a micrometeorite. The white contour delineates the height corresponding to 5% of the maximum height measured by AFM. Top right: AFM-IR spectra (labelled S1 to S4) obtained at the selected locations marked in the left panel. The vertical lines identify the 1710 cm^{-1} and 1600 cm^{-1} wavenumber positions. Bottom right: Histogram of the AFM-IR ratio map in the left panel, highlighting the strong heterogeneity of the sample.[46] These AFM-IR experiments were obtained in tapping-mode. This figure has been reproduced from D. Partouche *et al.* (ref. 46) with permission from ESP Sciences, copyright 2020.

by monitoring carbonyl absorption (absent in pristine parchment).[108] Morsch *et al.* used AFM-IR to study the UV-induced degradation of model linseed oil paints containing anatase (which has a high photocatalytic activity) and rutile; two TiO_2 polymorphs.[79]

Oil paints are made by mixtures of drying oils, pigments and additives (*i.e.* Al-stearate) that together provide desirable properties but are not indefinitely stable, as they can react to form metal carboxylates (soaps) that may damage works of art over time. Despite their common occurrence, soap formation and aggregation are not well-understood processes. Ma *et al.* used tapping-mode AFM-IR on a 23 year old naturally aged commercial paint of known average formulation to reveal that the distribution of metal carboxylates is heterogeneous at the nanoscale and more complex than previously thought.[17] For example, three distinct metal carboxylates were identified around a single agglomerate of the aluminum stearate additive (Fig. 11) providing valuable details to infer soap formation mechanisms. From these first experiments, AFM-IR clearly offer rich and valuable information while requiring just a very small amount of material, an ideal combination for cultural heritage applications.

4. Nano-Raman: fundamental principles of TERS

Nanoscale Raman spectroscopy, also known as tip-enhanced Raman spectroscopy (TERS), uses atomic force microscopy (AFM) or scanning tunneling microscopy (STM) to scan a plasmonic metal nanostructure over a sample surface, to locally enhance the field in a manner analogous to surface-enhanced Raman spectroscopy (SERS).[109–111] Such metallic nanostructures are typically produced by metal coating of nonconductive AFM tips or electrochemically etching conductive STM wire tips. In TERS experiments, the probe tip is positioned above the sample and a laser excites the particle's localized surface plasmon resonance (LSPR), a coherent oscillation of conduction electrons. The LSPR drastically enhances (up to 100–1000 fold) the local electric field (E) in the nanoparticle's vicinity, leading to Raman signal enhancements of up to 10^8.[112–114] The LSPR can be described by the solution the of Maxwell equations, also known as Mie theory, according to (eqn (9)):

$$E(\lambda) = \frac{24\pi^2 N a^3 \varepsilon_{out}{}^{3/2}}{\lambda \ln(10)} \left[\frac{\varepsilon_i(\lambda)}{(\varepsilon_r(\lambda) + 2\varepsilon_{out})^2 + \varepsilon_i(\lambda)^2} \right] \quad (9)$$

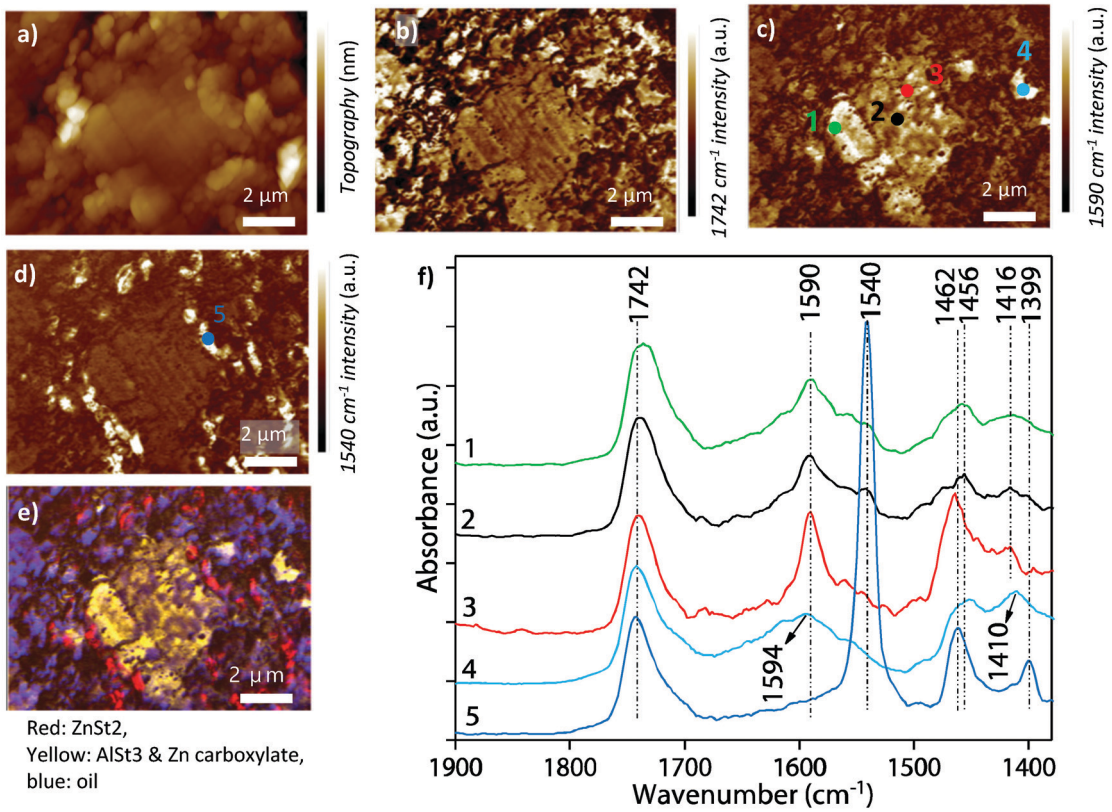

Fig. 11 (a) AFM topography and (b–d) AFM-IR absorption maps of 23 year old naturally aged commercial paint chip of known composition (zinc white containing pre-tested soft titanium white (P250) prepared at the Grumbacher paint factory in 1995). (b) AFM-IR map at 1742 cm^{-1} corresponding to the ν(C=O) marker band of oil, (c) PTIR map at 1590 cm^{-1} corresponding to a broad zinc carboxylate and (d) AFM-IR map at 1540 cm^{-1} corresponding to the carboxylate peak of zinc stearate. (e) Reconstructed qualitative color-coded image of PTIR absorption intensity: zinc stearate (red), "broad zinc carboxylate" (yellow) and oil (blue). (f) AFM-IR spectra obtained at the color-coded marked locations (1–5). The spectra are normalized to the ester carbonyl band at 1742 cm^{-1} and displayed with an offset for clarity. These AFM-IR experiments were obtained in tapping-mode. This figure has been reproduced from X. Ma *et al.* (ref. 17) with permission from Wiley, copyright 2019.[17]

where a is the nanoparticle radius, ε_r and ε_i are the real and imaginary components of the metal dielectric function; ε_{out} is a wavelength independent dielectric constant of the environment surrounding nanoparticles; λ is the excitation wavelength; N is the number density of the nanoparticles. Gold and silver nanostructures are commonly used as TERS probes since their plasmon resonance condition ($\varepsilon_r \approx -2\cdot\varepsilon_{out}$) is met in the visible spectral region. Other metals, such as Cu, Al, Pt, Pd, Ga, In, and Rh, and their alloys can potentially be used as plasmonic materials.[115–118] However, the feasibility of their application in TERS has not yet been fully explored.

Gold deposited on silicon or on glass is also often used as a substrate to achieve so called "gap-mode" TERS to obtain additional enhancement.[119] Alternatively, whole Au crystals[120] or Au nanoplates[121,122] can be used. Sheremet *et al.* compared the intensity of TERS spectra acquired from cobalt phthalocyanine on and off Au film[123] and found a ≈2-fold signal increase in the "gap-mode" TERS conditions.

The LSPR also depends on the size of the plasmonic nanostructure (see eqn (7)).[112–114] As a rule of thumb, the larger a nanoparticle, the bigger the LSPR red-shift. It should be noted that nanostructures on the tip of scanning probes are typically formed either by metal evaporation (for AFM-TERS) or by electrochemical etching (for STM-TERS), methods that offer very little control on the tip shape and size. Therefore, the LSPR and the enhancement factor in TERS typically show a strong tip-to-tip variability. Several strategies have been proposed to overcome this challenge. The Ren group developed a pulsed electrodeposition technique, which enables precise control of the deposited metal thickness by controlling the deposition current, potential, and time.[124] This wet chemistry-based method yields TERS probes within minutes without requiring sophisticated thermal deposition systems. For TERS experiments carried out under electrochemical control (usually with STM feedback), it is imperative that the shaft of the probe is covered with an insulating layer to avoid spurious Faraday currents. Various methods have been employed to achieve this,[125–127] many of them difficult to reproduce reliably, *i.e.*, requiring an experienced and very skilled experimenter. Finally, several microfabrication methods have been proposed for manufacturing TERS probes with a tapered waveguide on the tip[128,129] to allow for more a efficient coupling of the excitation laser light to the tip apex. However, nanofabrication of TERS tips is a slow process and thus less desirable than batch fabrication methods. For a more detailed discussion on TERS scanning probes and on novel fabrication strategies we refer the reader to a recent review by Huang and co-authors.[68]

The tip–sample distance is a key factor that affects the electromagnetic field confinement at the tip apex and for achieving the strongest TERS enhancement. When the tip is located far away from the sample surface, the field distribution is primarily determined by the tip radius.[130] However, the electromagnetic field becomes much more confined (Fig. 12) if a metallic substrate is in close proximity to the tip. Not only the proximity, but also the detailed structure of the tip apex plays a role for achieving extreme confinement of the

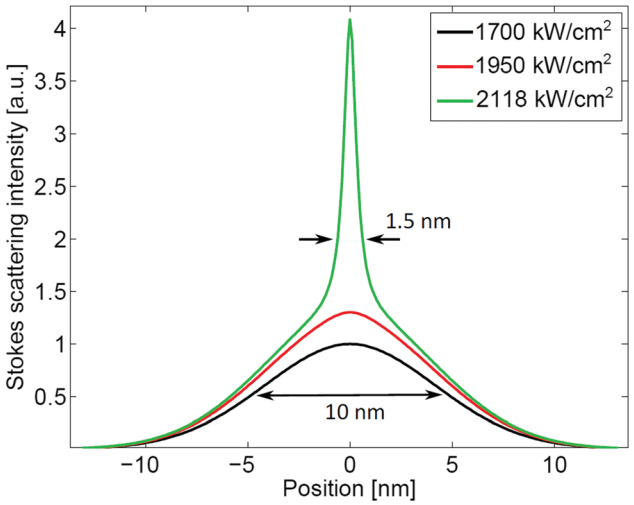

Fig. 12 Super-resolution in TERS. Computed Stokes scattering intensity as a function of lateral position assuming a point-source scatterer located at the origin and a Gaussian plasmonic field distribution of 10 nm full-width at half maximum. Nonlinearity of the response leads to a sharp increase in spatial resolution (green curve).[134] Copyright (2015) Nature Springer, reproduced with permission from Roelli *et al.*, *Nat. Nanotechnol.*, 2015, **11**, 164.

electromagnetic field in the tip–sample junction. It has been hypothesized that a tiny "supertip" could form a picocavity,[131] which is thought to be at the origin of the recently obtained TERS sub-nanometer spatial resolution.[132,133] At room temperature, metallic nanostructures are sufficiently plastic and not expected to be stable for extended periods of time, whereas at cryogenic temperatures, sub-nanometer resolution TERS is expected to be much more reproducible.

Zhang and co-workers investigated the relationship between the enhancement factor (EF) and the tip–sample distance.[135] It was found that the EF increases when the tip–sample distance increases from 0.25 nm to ≈1 nm, and the EF slowly decreases for larger distances. The increase of the EF in 0.25 nm to ≈1 nm tip–sample distance is explained by quantum effects that include electron tunneling and the appearance of a new charge-transfer plasmon modes. The decrease in the EF with increasing tip–sample gap above 1 nm is well characterized. For example, Masango and co-workers used atomic layer deposition to control the gap between a plamonic substrate and the analyte.[136] These researchers measured Al–CH_3 and C–H stretching modes from trimethylaluminum (TMA) as a function of the gap size and found that the SERS intensity decreased by more than 80% if the distance between the analyte and the plamonic surface was increased by only 0.7 nm (Fig. 13A). It was also found that the SERS intensity decreased less rapidly for gaps larger than 1 nm and reached ≈7% of the maximum for a gap of ≈3 nm.

These results provide the basis of a possible explanation for the absence of the amide I band in some SERS and TERS data:[137] Kurouski *et al.* analyzed the frequency of observing Cys, Phe, Tyr, Pro, and His bands in SERS spectra of native insulin with a decreased amide I band intensity (red), and with an

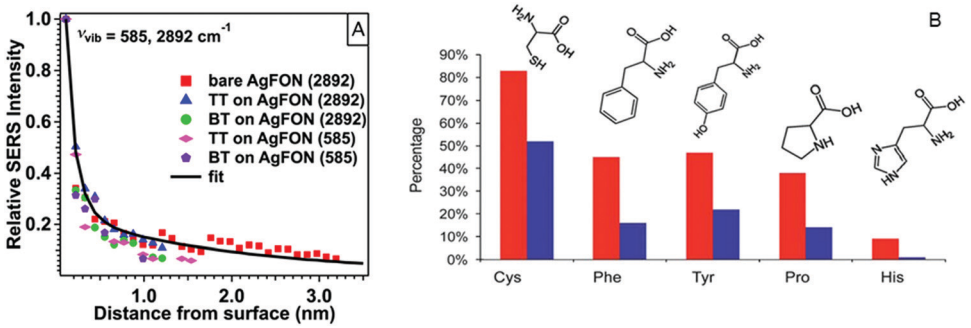

Fig. 13 (A) Normalized SERS intensity of the symmetric C–H stretch (from TMA) at 2892 cm^{-1} and symmetric Al–CH_3 stretch at 585 cm^{-1} as a function of distance from a bare silver film over nanoparticle (AgFON) and the substrate functionalized with thiol SAMs. (B) Propensities of cysteine (Cys), phenylalanine (Phe), tyrosine (Tyr), proline (Pro) and histidine (His) in SERS spectra of native insulin with a silent amide I band (red), and intense amide I (blue). (A) Reprinted with permission from Masango *et al.*, *Nano Lett.*, 2016. Copyright (2016) American Chemical Society. (B) Reproduced from Kurouski *et al.*, *Analyst*, 2013 with permission from The Royal Society of Chemistry.

intense amide I band (blue) (Fig. 13B). It was found that Cys was 1.5 times more prevalent in SERS spectra with the amide I band absent compared to the spectra with an intense amide I vibration. The ratio for Tyr was nearly 2 : 1 and further increased for Phe and Pro (almost 3 : 1). Histidine (His) was 9 times more frequent in the spectra with attenuated amide I band than with intense Amide I band (9 : 1) (Fig. 13B). The interpretation was that bulkier amino acid side chains act as 'spacers' between the peptide bond and the metal surface, and reduce the enhancement of the amide bond.[137] However, it is uncertain whether the orientation of the peptide backbond with respect to the enhancing SERS metal nanostructure is such that the side chain would automatically act as a spacer. More recently, it was found that high illumination intensities in TERS creates hot carriers under the tip, which cleave the peptid backbone, in a fashion analogous to electron capture dissociation of peptides in mass spectrometry.[138] This provides an alternative interpretation of the phenomenon, suggesting that simply controlling the illumination power could mitigate this effect.

In addition to the electromagnetic enhancement, chemical enhancement can also play a role in TERS.[119] Chemical enhancement is associated with a charge transfer occurring from the Fermi level of the metal tip to the lowest unoccupied molecular orbital of a bound analyte. Valley and co-workers performed a careful theoretical and experimental study to quantify the effect of the charge transfer[139] on the EF of plasmonic nanostructures and found that the chemical enhancement provides an EF from 10 to 100.

TERS instruments have been implemented in several optical configurations, Fig. 14. Bottom-illumination TERS is commonly used for TERS imaging of biological samples.[122,140] In this configuration, the laser light is focused on the tip by oil-immersion or dry microscope objective with high numerical aperture (NA) which allows to collect the scattered photons efficiently and consequently permits efficient TERS imaging. However, this configuration can only be used to measure transparent samples. This limitation can be overcome by setups leveraging side- or top-illumination.[141] Side illumination is commonly used in electrochemical[126,127] and ultra-high

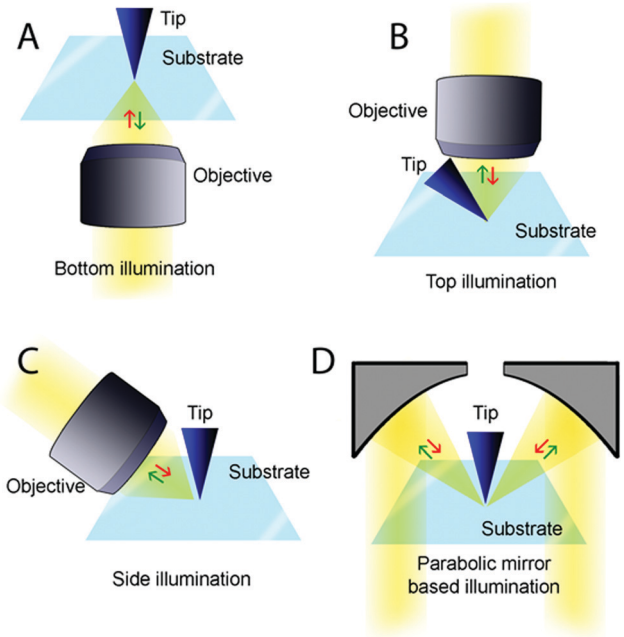

Fig. 14 Bottom- (A), top- (B), and side-illumination (C) configurations, as well as a parabolic mirror-based setup (D) used in TERS systems.

vacuum TERS systems.[142–144] In these systems, light focusing is achieved either *via* a standard microscope objective or by a set of achromatic lenses or, alternatively, by a parabolic mirror.[145] Although in theory such focusing geometry enables highly efficient light collection, parabolic mirror-based experimental setups did not gain much popularity due to higher complexity for alignment and focusing.

Continuous wavelength (CW) laser light is commonly used in all configurations of TERS systems.[141,146–149] Several attempts have been made to use pulsed sources for TERS.[150,151] But these did not yield new or additional information compared to TERS experiments carried out with CW excitations. Nevertheless, the realization of time-resolved TERS is in principle of broad interest and it has recently been implemented.[152]

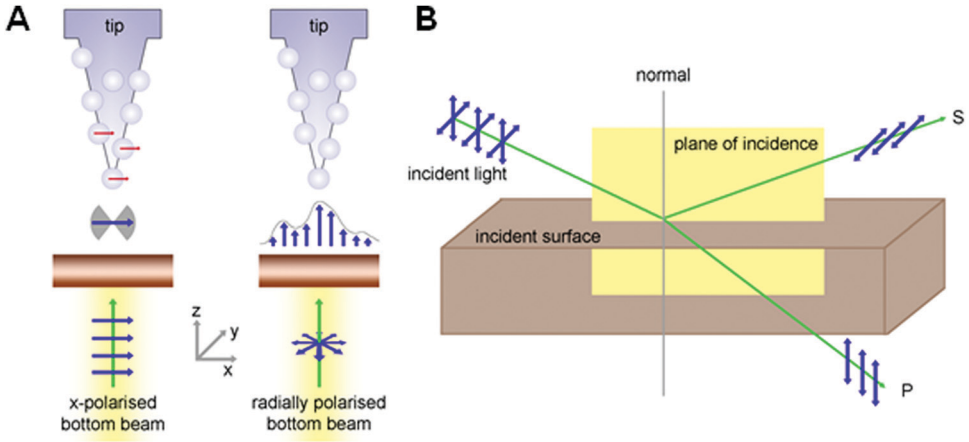

Fig. 15 (A) Schematic representations of polarization at the sample surface for linearly and radially polarized light used in bottom-illumination. The blue arrows represent the polarization of the field of the incoming beam and at the tip and sample surfaces. The red arrows show the induced polarization of plasmons on the metallic particles covering the tip. (B) Definition of S and P polarized light upon side-illumination TERS.

The use of polarizers allows controlling linear or circular light polarization at the tip–sample junction (Fig. 15A);[153] however the importance of laser light polarization in TERS experiments has not been fully explored and is currently an open question. In side-illumination geometries (Fig. 15B), light can have p- (electric field parallel to scattering plane) and s-polarization (electric field perpendicular to scattering plane). It is expected that the laser light with polarization along the tip axis (p-polarization) would provide the highest electromagnetic enhancement.[154] Similarly, for bottom-illumination TERS light polarization along the tip axis (*z*-polarized light) is expected to provide the highest enhancement.[154] While the vertical polarization component increases with larger illumination angles (*i.e.*, higher NA objectives) experimental evidence suggest that strong TERS enhancement can be obtained even with low NA objectives.[155]

An interesting study on the effect of light polarization in TERS experiments had been reported by Pashaee and co-workers that investigated the near-field response of azobenzenethiol adsorbed on gold nanoplates using linearly and radially polarized light,[156] with the latter yielding 3 times greater TERS signal intensity.

5. Recent advances and practical application of TERS

Five major research directions have been actively pursued by the TERS community over the last two decades: (1) single molecule sensitivity and improvement of spatial resolution, (2) structure and dynamics of biological systems, (3) materials characterization, (4) electrochemistry and (5) catalysis at the nanoscale.

5.1 Single molecule sensitivity and spatial resolution

Sensitivity and spatial resolution are linked: the smaller the area that is probed by the TERS tip, the fewer molecules are under the tip; at the extreme (resolution of <1 nm) there is only a single molecule. The first TERS report with single molecule sensitivity came from the Pettinger laboratory. These researchers claimed detection of a single brilliant cresyl blue (BCB) molecule adsorbed on a 12 nm thick Au film using an electrochemically-etched silver wire probe.[157] This report, however, raised numerous speculations about the detection accuracy. To end such speculations, the Van Duyne group employed isotopologues of Rhodamine 6G (R6G) and confirmed the single-molecule sensitivity of TERS[153] by showing that the vibrational signature of only one R6G isotopologue could be observed at a given time in multiple TERS spectra. Although single molecule sensitivity with poor (non-resonant) Raman scatterers has not yet been achieved. Single molecule sensitivity with resonant dye molecules (TERRS) can thus be considered to be established.

Over the last two decades, TERS attained giant improvement in spatial resolution. In 2000, Stöckle *et al.* anticipated that TERS spatial resolution would be limited by a size of the scanning probe (30 nm to 50 nm).[110] However, very soon, experimental evidence revealed a much better spatial resolution. For instance, the Kawata group reported images of carbon nanotubes (CNTs) with less than 2 nm spatial resolution, sufficient to identify various defects on the CNT surfaces.[158] Using low-temperature UHV-STM-TERS, Zhang and co-workers recently demonstrated that adenine and thymine bases adsorbed to Ag(111) could be resolved with $\approx$1 nm spatial resolution.[159] Under low temperature, the mobility of molecules on the substrate can be minimized, trapping them in the most energetically favorable configurations. In 2013, the Dong group reported the first sub-nanometer spatial resolution of TERS by resolving the inner structure and surface configuration of a porphyrin molecule (H_2TBPP).[133] These researchers suggested that such a high spatial resolution was likely due to a resonance between the nanocavity plasmon and the molecule vibronic transitions, particularly of the downward transition responsible for the emission of Raman photons.[133] Several years ago, Chaing and co-workers demonstrated

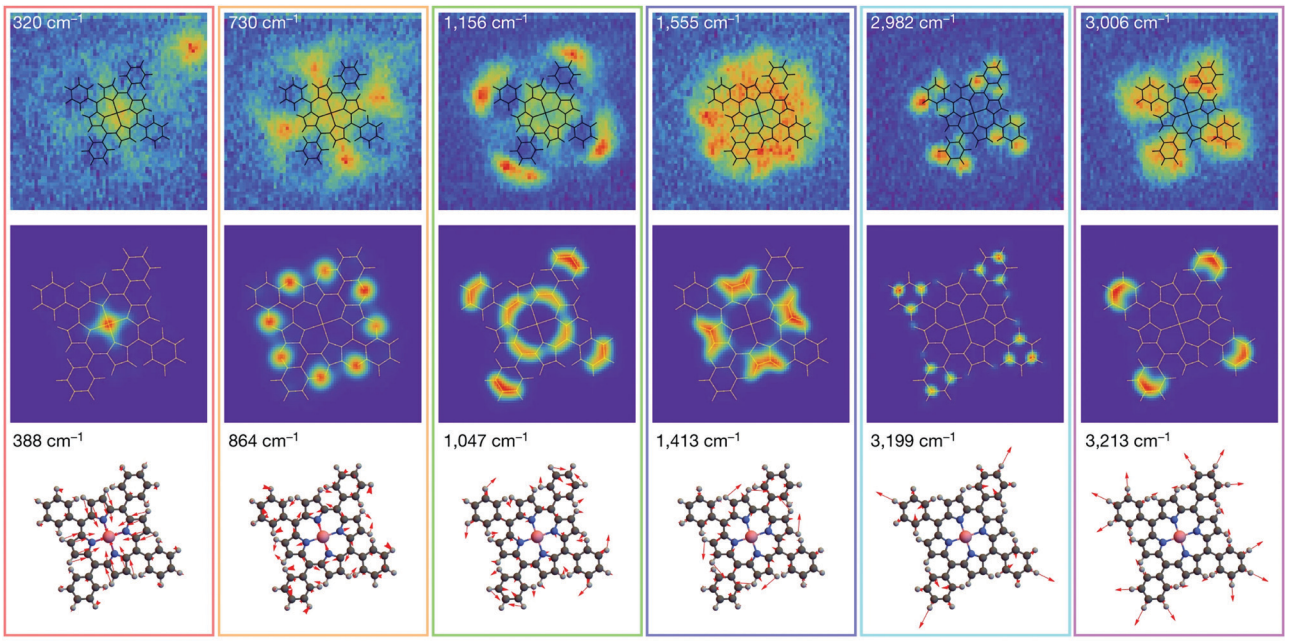

Fig. 16 TERS images (top row) of individual CoTPP molecule allows for visualization of vibrational normal modes (middle and bottom rows). Reproduced from Lee *et al.*, *Nature*, 2019, with permission from Nature Publishing Group.

Angstrom spatial resolution on H_2TBPP adsorbed on a Cu(111) surface in UHV-TERS. The H_2TBPP/Cu(111) system revealed two metastable surface-mediated conformations: buckled up and buckled down. These researchers demonstrated that at room temperature, the conformational barrier can be easily overcome and that H_2TBPP randomly switches between these two states. Simultaneous measurement of STM and TERS line scans across four H_2TBPP molecules showed a 2.6 Å TERS lateral resolution.[144] The spatial resolution of TERS was pushed even further by the Apkarian group: Lee and co-workers recently reported TERS images of individual Co(II)-tetraphenyl porphyrin (CoTPP) molecule obtained with <2 Å spatial resolution showing that TERS can probe the inner structure of a molecule, such as its mechanical motions and internal electric currents (Fig. 16).[132] The same group also demonstrated that a comparable TERS spatial resolution could be achieved using a carbon monoxide (CO)-modified scanning probe.[160] It was concluded that field localization, rather than the enhancement, is the crucial factor for single molecule sensitivity and sub-nanometer spatial resolution. At this extreme confinement, plane-wave selection rules break down and field gradients driven scattering dominates the observable TERS spectra.

There have also been claims of nanometer or even subnanometer spatial resolution with ambient TERS. Deckert-Gaudig and co-workers demonstrated $\approx$1.5 nm spatial resolution for AFM-TERS and established the technique capability for detecting individual amino acids on the surface of single insulin fibrils.[140] Also, the Deckert group attempted to reach <1 nm spatial resolution using TERS for sequencing specifically designed single-stranded DNA (ssDNA) composed of adenine and cytosine.[161] However, such high-resolution TERS proved extremely difficult to reproduce. At present, there is only one other report in the literature where a silver tip was scanned along a ssDNA to collect TERS signals with a step of 0.5 nm, comparable to the bond length between two adjacent DNA bases.[162] The difficulties arise from four aspects: (i) non-conductive biological samples can only be measured with AFM-TERS, which has less enhancement; (ii), biological molecules such as proteins or DNA have much lower Raman scattering cross sections than the resonant dyes commonly investigated in single-molecule TERS, making their detection challenging; (iii) the larger drift at ambient temperature than in cryogenic conditions, renders TERS imaging with long pixel integration times challenging; and (iv) the "supertips" or picocavities required for very high TERS resolution are not stable at room temperature.

Two years ago, the Kurouski group reported the first three dimensional (3D) TERS, which could be achieved by active plasmon zones located on a shaft of the scanning probe. Wang and Kurouski utilized 3D TERS to monitor the reduction of *para*-nitrothiophenol (pNTP) molecules (pNTP) catalyzed by Au microplates.[121] The results showed that the 3D TERS could distinguish signals from both the side and plateau regions of single Au microplates, corresponding to Au(100)[163] or Au(110)[164] with low catalytic activity and Au(111) with higher catalytic activity, respectively, Fig. 17.

5.2 Structure of biological systems

During the last two decades, TERS was widely used to explore the structure of biological systems. Although many questions remain unanswered, TERS substantially improved our understanding of the structural organization of numerous biological assemblies such as amyloid and collagen fibrils. Some attempts have also been made to read DNA and RNA nucleotide

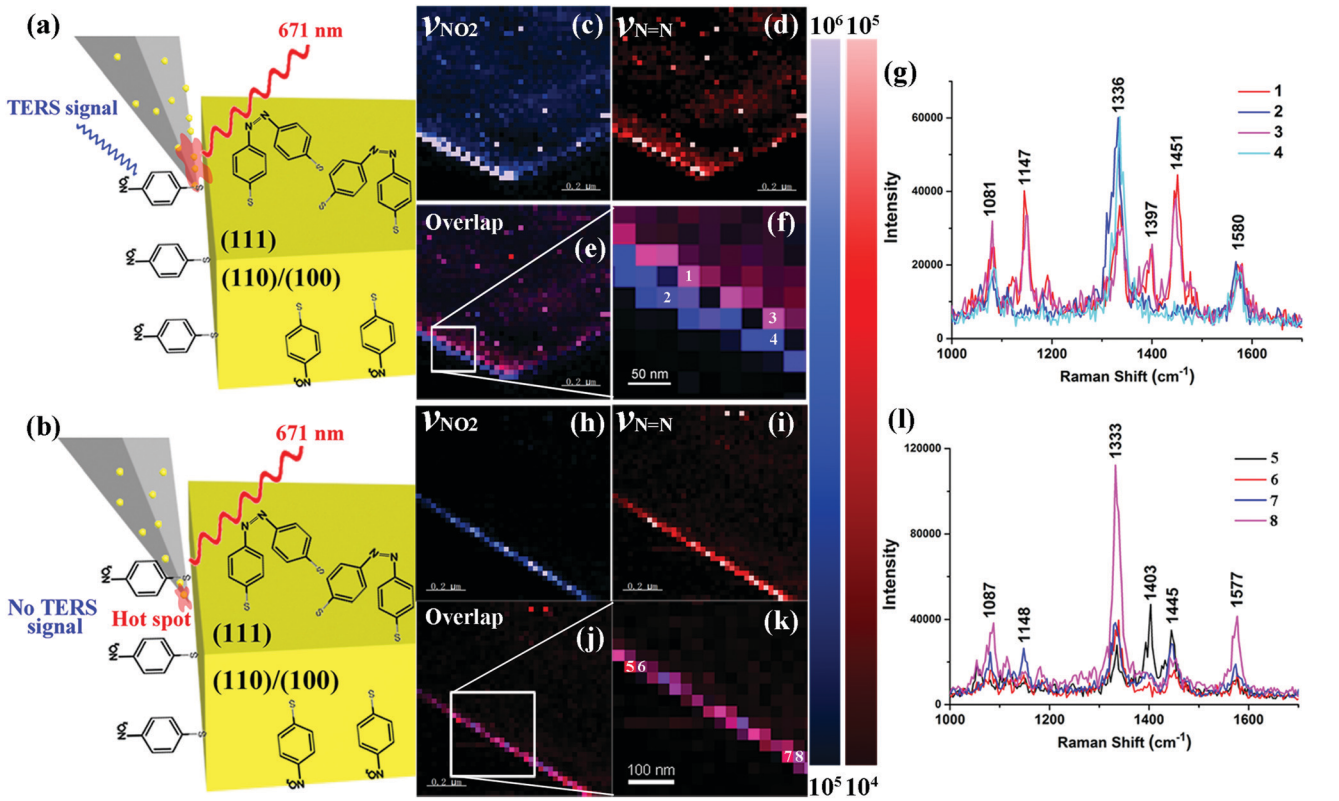

Fig. 17 TERS imaging of the facet-dependent reduction of pNTP catalyzed by Au microplates. (a and b) Proposed schemes showing the hot-spot located at both the shaft and apex (a) and only at the apex (b) of the TERS probe. (c, d) and (h, i) High resolution TERS images of the distribution of $-NO_2$ (c and h) and N═N groups (d and i) obtained with 3D TERS active and inactive probes respectively. (e and j) Corresponding overlap of NO_2 and N═N images (c and d for e; h and i for j). (f and k) Zoomed-in TERS images of the white rectangle position in (e) and (j), respectively. (g and l) Typical TERS spectra extracted from the marked position in (f) and (k). Reprinted with permission from Wang and Kurouski, *J. Phys. Chem. C*, 2018. Copyright (2018) American Chemical Society.

sequences[140,147,165] and even to probe the surface of cells and viruses. Unfortunately, many biomolecules are poor Raman scatterers, which leads to difficulties. The temptation is to simply raise the excitation laser power to generate more Raman scattering, but this can lead to decomposition. If one works at sufficiently low laser power, long integration times are required, which leads to slow imaging rates and problems with drift.

DNA sequencing is a bottleneck of modern genomics and bioinformatics. Therefore, alternative methods of DNA and RNA sequencing are highly desired. In 2010, Treffer and co-workers proposed to use TERS to read individual nucleobases on a single stranded calf thymus DNA with an arbitrary sequence.[147,148] The authors showed that the four nucleobases exhibited distinctly different vibrational signatures that could in principle be used for DNA and RNA sequencing.[166,167] This work was further expanded by Najjar and co-workers who were able to read the DNA of a λ-phage virus with TERS. Although the authors revealed vibrational modes originating from DNA nucleobases and from the DNA backbone, the reported 9 nm spatial resolution significantly limited base-by-base readout necessary for DNA sequencing.[168] Several years later, Pashaee and co-workers used TERS to distinguish between plasmid-free and plasmid-embedded DNA molecules[169] thanks to the stronger TERS signals from plasmid DNA which contributes additional nucleic acids from the plasmid. Lipiec and co-workers utilized TERS to investigate mechanisms of UV-initiated DNA damage. Experimental evidence suggested that such DNA damage occurred *via* cleavage of the C═O bonds.[170]

Amyloid fibrils are protein aggregates that may develop from misfolded proteins causing several neurodegenerative maladies such as Alzheimer and Parkinson diseases.[171] Although their structure has been revealed by cryo-EM and solid-state NMR, the surface organization of these aggregates, to a large extent, remained unclear. In 2012, Deckert-Gaudig and co-workers proposed to use TERS to probe the amino acid composition on the surface of insulin fibrils.[140] Additionally, these researchers showed that TERS could be used to probe changes in protein secondary structure on the surface of insulin fibrils. Following on this work, Kurouski and co-workers reported a more detailed study on the structural organization of insulin fibrils.[140] These researchers were able to correlate the propensity of the presence of cysteine, proline, phenylalanine, tyrosine and histidine amino acids with the protein secondary structure. It was found that tyrosine, phenylalanine and cysteine were more frequently present on β-sheet clusters comparing to the areas dominated by α-helix and/or unordered protein. Consistently, proline, which is known to disrupt β-sheet integrity, was much more

abundantly observed in α-helix and/or unordered protein clusters. Kurouski and co-workers also examined the structural organization of filaments, precursors of amyloid fibrils that intertwine and coil forming mature protein aggregates. This information allowed them to propose two distinctly different protein aggregation pathways that led to the formation of twisted and tape-like fibrils. Deckert-Gaudig and co-workers used TERS to image hydrophobic and hydrophilic domains on the surface of insulin fibrils, as well as to reveal clusters of specific amino acids, such as cysteine and proline.[172] It was found that the surface of insulin fibrils is composed of a mixture of α-helix and disordered protein secondary structures, whereas the core of the fibrils consists exclusively of β-sheets.

Recently, Bonhommeau and co-workers investigated the structural organization of two synthetic mutants of $A\beta_{1-42}$ fibrils using TERS. They collected spectra from the surface of normal $A\beta_{1-42}$ fibrils and fibrils formed from a peptide with leucine to threonine mutation at the 34th residue (L34T) fibrils, which exhibited low toxicity. Next, these researchers compared these spectra to the spectra collected from surfaces of highly toxic oligomers (oG37C)[173] determining that $A\beta_{1-42}$ and L34T fibrils secondary structure consisted of parallel β-sheet, while the Og37C secondary structure consisted of anti-parallel β-sheets. The structural organization of $A\beta_{1-42}$ fibrils was further elucidated by the Zenobi group with TERS,[149] to reveal the spatial distribution of the secondary structure (β-sheet and turn/random coil) in fibrillar species at different stages of maturation. These researchers also imaged large areas of mature $A\beta_{1-42}$ fibrils showing the distribution of β-sheet and turn/random coil protein secondary structure on their surface. An interesting application of TERS was reported by Van den Akker and co-workers which probed the structural organization of fibrils formed on a lipid interface.[174] It was found that fibrils grown on the lipid interface contained lipid molecules on their surface. Tabatabaei and co-workers were able to image amyloid β plaques on the surface of neuronal spines using TERS.[175] The plaques have highly heterogeneous protein secondary structure, including disordered, α-helical and β-sheet structures.

Fibril polymorphs are morphologically and/or structurally different protein aggregates that can be grown from the same monomeric protein or a polypeptide.[176,177] It was proposed that fibril polymorphism could be caused by variations in monomer–monomer aggregation at the stage of protein nucleation or by different association pathways of fibril filaments and protofibrils.[178,179] Kurouski and co-workers utilized TERS to probe the surface organization of insulin fibril polymorphs with different topologies: tape-like and twisted fibrils.[180] It was found that surfaces of these polymorphs had distinctively different amino acid compositions and protein secondary structures. This work was further expanded by Krasnoslobodtsev and co-workers who investigated polymorphism of amyloid fibrils formed by an eight amino acid peptide (CGNNQQNY) from the yeast prion protein Sup35.[181] It was found that the fibril polymorph grown at pH 5.6 had a mixture of β-sheets, random coil and α-helix structures, whereas fibrils grown at pH ≈ 2 were primarily composed of β-sheets.

Imaging the spatial organization of cell surfaces is an important, but challenging, longer-term goal of many labs using TERS. For example, in malaria, a severe insect-transmitted tropical disease that is caused by *Plasmodium falciparum*, the parasite lives inside red blood cells turning erythrocyte hemoglobin into hemozoin and free heme. The Wood group used TERS to detect hemozoin crystals inside the red blood cells[182] and to determine the oxidation state of iron ions inside such crystals. A similar application of TERS was reported by Böhme and co-workers. These authors provided experimental evidence that TERS could be used to probe the oxidation states of cytochrome-*c* Fe^{2+}/Fe^{3+} in a single isolated mitochondrion.[183] Recently, Xiao and co-workers showed that TERS can unravel chemical information on specific ligand–receptor binding sites of the integrin $\alpha_v\beta_3$ molecule in a cancer cell membrane.[184] These researchers were able to obtain distinct Raman signals using gold nanoparticles (located on the substrate) functionalized with three different peptide ligands. Böhme and co-workers made several attempts to probe the structural organization of cell membrane using TERS which revealed individual protein and lipid domains on the surface of eukaryotic cell[147] and oligosaccharides on the cell surface.

5.3 TERS imaging of 2D materials

TERS was actively used to investigate the structure and composition of graphene and its derivatives.[185–187] For instance, Schaffel and co-workers used TERS to detect small defects and localized contaminations in graphene sheets and showed that the intensity of the D band (1350 cm^{-1}) significantly increases at graphene edges and in defect-rich areas.[188] In contrast, in-plane modes, such as the G band (≈1582 cm^{-1}), were found to be weakly enhanced in TERS.[189] TERS was also used to study chemically modified graphene oxide,[190] specifically to investigate the electronic properties of a carboxyl-modified graphene oxide (GO–COOH) and localized functional groups on its surface. The researchers were able to detect nanoscale defects by comparison of intensities of G and D bands in thick and thin layer GO–COOH flakes Fig. 18.

Chemical vapor deposition synthesis allows manufacturing a multitude of transition metal dichalcogenides (TMDs), such as $NbSe_2$, MoS_2, $MoSe_2$, WS_2, WSe_2, and TaS_2. Although structurally very similar, they all have unique electronic properties. Since nanoscale defects, adatoms, vacancies and other structural heterogeneities in these TMDCs may significantly change the lattice symmetry-induced valley Hall effect, valley polarization, and superconductivity it is very important to understanding the structural organization of these materials at the nanoscale. TERS and tip-enhanced photoluminescence (TEPL) are ideal for such applications; compared to organic or biological molecules, dichalcogenides are more robust and tolerate higher laser powers. For instance, Park and co-workers showed that TERS and TEPL coupled to atomic force local strain microscopy could be used to image the surface of WS_2 and investigate its excitonic properties.[130] Milekhin and co-workers observed strong hot-electron doping in MoS_2 when the material is deposited on Au nanoplates which induces a structural transition from the 2H to the 1T phase.[191]

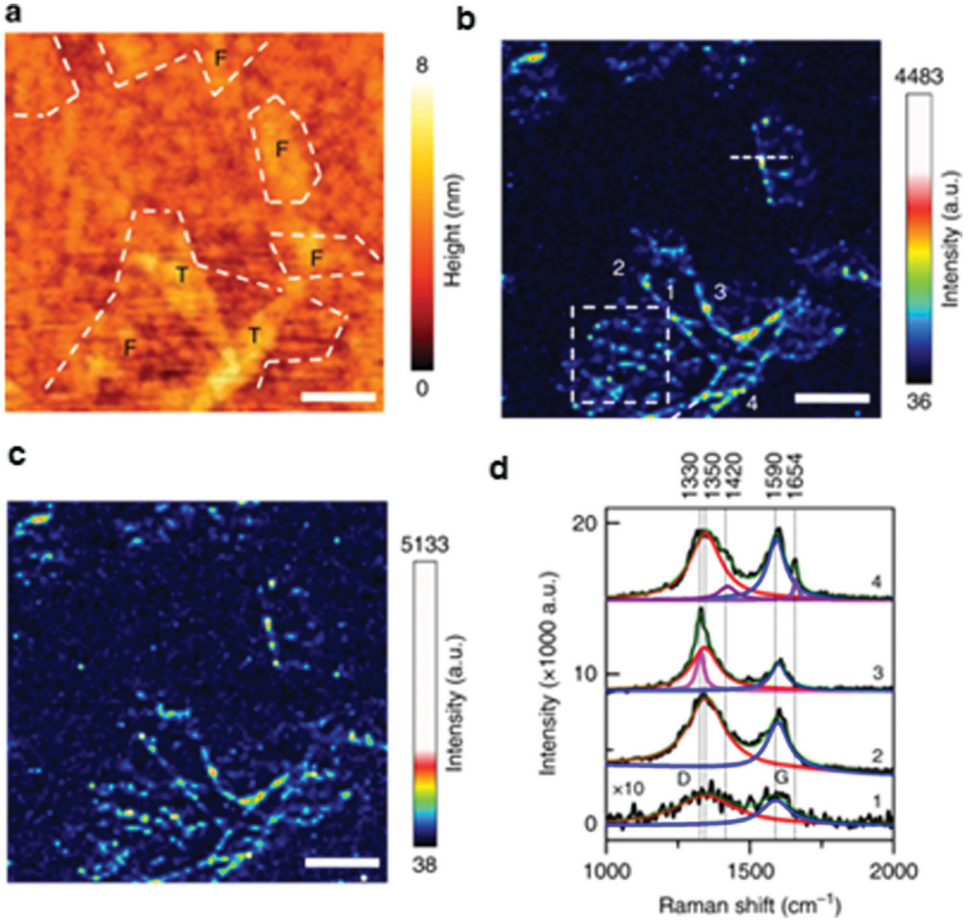

Fig. 18 High-resolution TERS mapping of a GO–COOH flake. (a) Topography map of a multilayer GO–COOH sample obtained simultaneously with TERS mapping. "T" and "F" refer to thick-layer and few-layer GO–COOH flakes, respectively. (b) TERS maps of D band (1350 cm^{-1}) intensity and (c) G band (1590 cm^{-1}) intensity measured from the GO–COOH sample area shown in (a). Nominal pixel dimension: 10 nm. Integration time: 0.4 s. (d) TERS spectra measured at the locations marked 1–4 in (b) along with the fitted Lorentzian curves. The intensity of the averaged TERS spectrum from location 1 was scaled by 10× for easier visualization. All scale bars: 200 nm. Reproduced from Su *et al.*, *Nat. Commun.*, 2018, with permission from Nature Publishing Group.

Organic 2D polymers. The Zenobi group applied TERS to elucidate the molecular mechanisms leading to the formation of two-dimensional organic molecular polymers. 2D polymers are difficult to investigate spectroscopically because these low-density materials are only one molecular layer thick. The sensitivity of TERS has made possible in recent years, to assess the crystallinity, defect density, and degree of polymerization of these materials based on high-resolution TERS images.[192] 2D polymers can be synthesized from monomers that will form strong noncovalent π–π interactions, for example, between partially fluorinated anthracene moieties,[193] or that form covalent bonds.[194] For example, Opilik *et al.*[195] and Müller *et al.*[196] determined that organic polymer films made from similar anthracene-based monomeric precursors formed *via* [4+4] rather than [4+2] cycloaddition reactions. Based on these results they hypothesized that such polymerization occurred *via* a step growth mechanism. This work was further expanded by Shao who used TERS to investigate polymers synthesized *via* dynamic imine chemistry from aromatic triamine and dialdehyde building blocks.[197,198] It was possible to determine the defect density in such a 2D polymer monolayer by using an acetylenic reporter group built into the dialdehyde monomer. Specifically, the researchers were imaging C≡C stretching (2220 cm^{-1}) in an intact 2D polymer sheet to identify locations of polymer defects (Fig. 19).

5.4 Electrochemical processes at the nanoscale

The nanoscale organization of species on electrode surfaces plays a key role in the efficiency of electrochemical and electrocatalytic processes at the solid–liquid interface.[199,200] The spatial resolution of classical spectroscopic techniques, such as ultraviolet-visible absorbance, fluorescence spectroscopy, IR and Raman spectroscopy, used to characterize electrochemical processes is diffraction limited, and therefore these techniques miss critical nanoscale details. Scanning electrochemical microscopy (SECM) and scanning electrochemical cell microscopy (SECCM) are commonly used to study electron transfer kinetics on a single crystal *vs.* polycrystalline substrates.[200–202] However, both techniques can provide only very little structural information about the analyzed molecules or directly probe

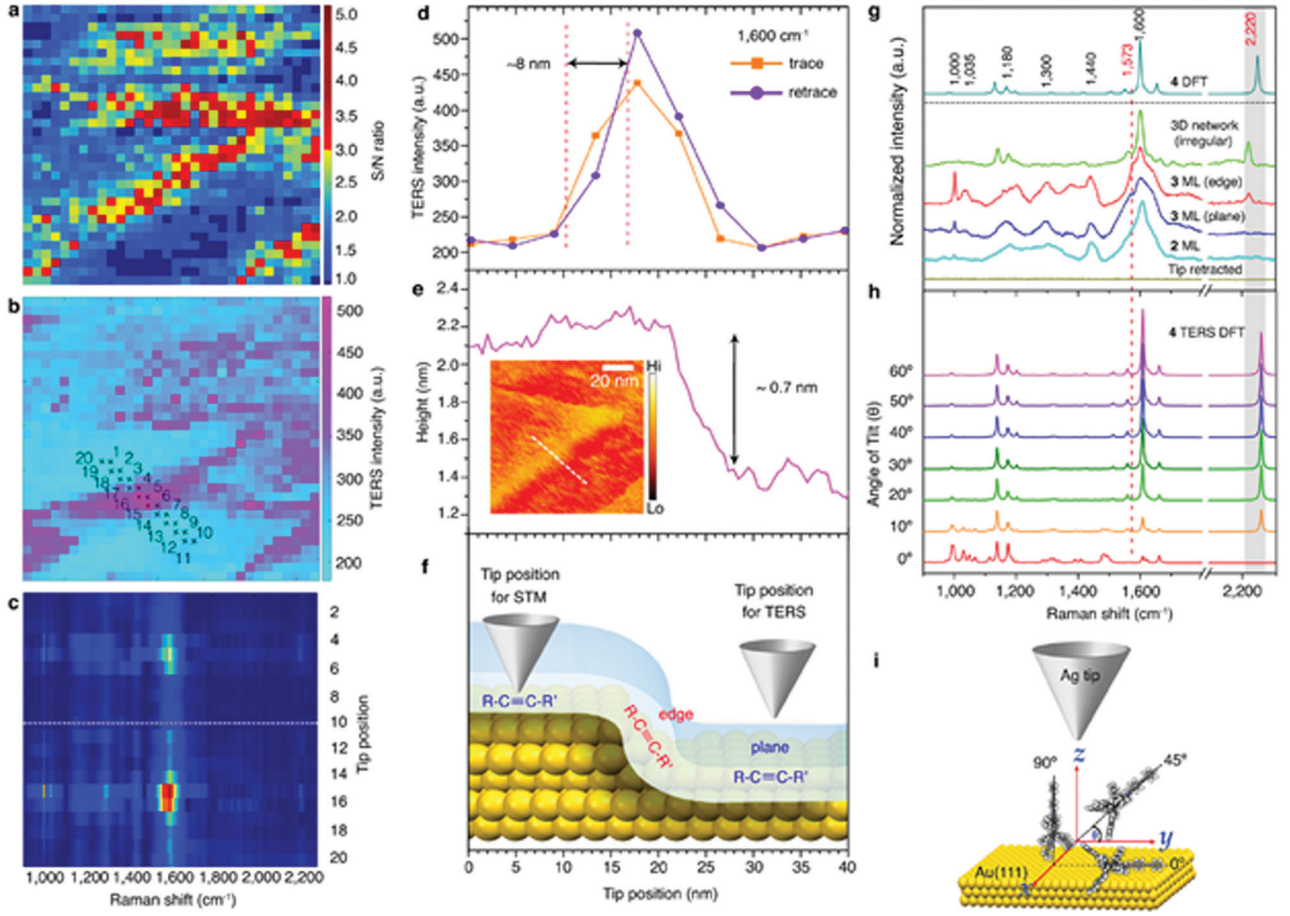

Fig. 19 TERS imaging and spectra of a 2D covalent monolayer obtained *via* imine bond formation by reacting a dialdehyde and a triamine. (a) TERS signal-to-noise ratio imaging the C≡C stretching (2220 cm^{-1}) in an intact 2D polymer sheet; (b) TERS intensity image at 1600 cm^{-1} of the ML on a terrace of the Au(111) substrate; (c) color-coded intensity map of two line-trace TERS scans taken in (b); (d) corresponding TERS intensity of the band at 1600 cm^{-1} along the trace and retrace scans. The spatial resolution is estimated to be around 8 nm using a 10% to 90% contrast criterion; (e) STM image and corresponding topographic height profile of the terrace after TERS imaging; (f) schematic of edge-induced molecular tilt within the ML. STM image (0.2 V, 1.0 nA) taken after TERS maps (0.2 V, 0.1 nA) with different parameters to avoid scratching the ML; (g) TERS spectra recorded from the ML on the plane and edge positions of Au(111) substrate; (h) calculated TERS spectra of imine model, normalized to the 1124 cm^{-1} band. (i) Schematics of the plane-parallel configuration and plane-perpendicular configuration, respectively. The molecular bending and twisting angles are held constant at 0°.[198] Reprinted with permission from F. Shao *et al.*, *ACS Nano*, 2018, **12**, 5021. Copyright (2018) American Chemical Society.

molecules that are bound to the surface. The Mirkin group has recently demonstrated that a spatial resolution as low as 10 nm could be achieved using SECM.[202] However, to better understand the fundamental principles of electrochemistry and of heterogeneous electrocatalysis clearly, the sub-nanometer spatial resolution offered by TERS is necessary.

The groups of Ren, Van Duyne and Domke have pioneered development of TERS to probe electrochemical processes at solid–liquid interfaces.[126,127,203] The Van Duyne group explored the nanoscale redox reaction of Nile Blue (NB) using electrochemical AFM-TERS (EC-AFM-TERS) and compared these results to conventional cyclic voltammetry (CV) (Fig. 18).[203] For this study, NB was absorbed onto an indium tin oxide (ITO) film that was used as a working electrode (WE) while Pt and Ag/AgCl were used as counter (CE) and reference (RE) electrodes, respectively. Next, an Au-coated AFM tip was positioned on the WE. At a pH value above 6, NB undergoes a two electron one proton reduction at negative potentials (approximately −0.5 V *vs.* Ag/AgCl). Therefore, changes in TERS spectra were monitored as the potential was swept from 0.0 V to −0.6 V *vs.* Ag/AgCl and back to 0.0 V *vs.* Ag/AgCl. Kurouski and co-workers found that the overall intensities of the spectra decreased with a decrease of the potential, in agreement with the change in electronic states of NB_O and NB_R. As the potential was swept from −0.6 V back to 0.0 V, ≈75% of the initial spectral intensity was recovered, demonstrating reversibility of the redox reaction of NB under the AFM tip, monitored by TERS.

These researchers also observed step-like changes of the TERS intensity of NB in some TERS voltammograms, such as the one shown in Fig. 20E. Such a step-like behavior of TERS CVs suggests that redox reactions of only a few NB molecules were probed at those surface sites, 6 based on the estimate of the average number of molecules under the tip. This study

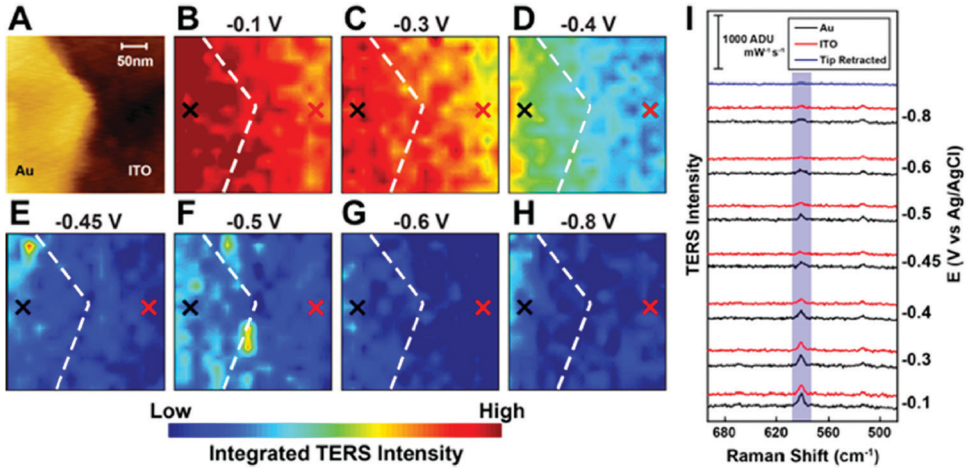

Fig. 20 (A) AFM image at the corner of an Au nanoplate on ITO (320 nm × 320 nm) and (B–H) corresponding TERS intensity maps (1 s acquisition time per pixel) of NB (591 cm^{-1} peak area) as a function of potential *vs.* Ag/AgCl. The white dotted lines represent the edge of the Au nanoplate. Each TERS pixel size is 20 nm × 20 nm. (I) Selected TERS spectra obtained on Au (black) and ITO (red) pixels as a function of the potential. The tip-retracted spectrum obtained after the imaging experiment is shown in blue. Reprinted with permission from Kang *et al., Nano Lett.,* 2018. Copyright (2019) American Chemical Society.

highlights the potential of TERS for studying redox reactions at the nanoscale, probing few- or single-molecule behavior across heterogeneous surfaces.[203] This work was followed by Mattei *et al.* demonstrating that EC-TERS could be used to measure nanoscale variations in the formal potential ($E^{0\prime}$) of a surface-bound redox couple.[204] These researchers acquired multiple TERS CVs at different surface coverages of NB on the surface of ITO and different locations on the ITO surface. Next, the TERS CVs were fit to a Laviron model for surface-bound electroactive species, which allowed for a quantitative extraction of the formal potential $E^{0\prime}$ at each location. Histograms of the single-molecule $E^{0\prime}$ at each coverage indicated that the electrochemical behavior of the cationic oxidized species is less sensitive to the local environment than the neutral reduced species.

The Van Duyne group recently demonstrated the first EC-TERS imaging monitoring changes in the formal potential ($E^{0\prime}$) of NB redox reaction on ITO and Au nanoplates.[205] These researchers observed a statistically significant 4 mV difference in $E^{0\prime}$ on Au *vs.* ITO and an electrochemical heterogeneity of redox events on polycrystalline ITO, but not on Au. EC-AFM-TERS imaging allowed for imaging of individual ITO grains with a spatial resolution of ≈40 nm, Fig. 20.

Independently, the Ren group leveraged EC-TERS to monitor the arrangements and to elucidate the protonation states of 4′-(pyridin-4-yl)biphenyl-4-yl)methanethiol (4-PBT) molecules on a Au(111) surface.[127] These researchers developed an elegant EC-STM-TERS setup with a tilted sample plate relative to the incident laser light. To reduce the Faraday current from the probe shaft, Zeng and co-workers embedded freshly-etched Au or Ag wire into a polyethylene glue, which preserved the activity of the plasmonic tip apex. Recently, Ren group demonstrated that the utilization of water immersion objective with a short working distance and high numerical aperture in EC-STM-TERS setup substantially improves the signal to noise ratio of the spectra.[206] This novel imaging approach, was used to investigate the redox properties of hydroquinone. It was found that more than a half of hydroquinone molecules could not be reversibly oxidized. This appeared to be a synergistic effect of negative potential and laser illumination rather than the tip LSPR that led to such an irreversible reaction.

Using EC-TERS, the Domke group examined the adsorption geometry and chemical reactivity of adenine on Au(111) as a function of applied potential.[126] The researchers demonstrated that protonated physisorbed adenine adopted a tilted orientation at low potentials while it was vertically adsorbed near the point of zero charge. A further increase in the potential induces adenine deprotonation and the reorientation to a planar configuration.[126] The Lucas group proposed an elegant experimental setup for STM-EC-TERS measurements,[141,146] using a very thin layer of liquid and a slightly bent tip to illuminate the tip with an objective located in air above the sample. Using a 4-nitrothiophenol layer assembled on large gold substrates they showed that the distribution of the surface transformation products could be heterogeneous.[141] Further exploring the possibility of top-access of EC-TERS, Touzalin and co-workers demonstrated EC-TERS with an objective immersed in the electrolyte solution. With this experimental setup, these researchers could track the progressive conversion of the nitro group of 4-NTP to amino (4-ATP). They found that the intermediate $4e^-$ reduction of the nitro group of 4-NTP to hydroxylamine (4-HATP) competes with a $6e^-$ reduction to amine (4-ATP) at potentials where this was not expected to occur.[146] The Lucas group demonstrated EC-TERS imaging of a Au surface functionalized with sodium sulfate with 8 nm spatial resolution.[207] Similar spatial resolution was achieved by the Domke group that used EC-TERS to investigate electrochemical oxidation of Au nanodefects.[208] The researchers observed reversible, concurrent formation of spatially separated Au_2O_3 and Au_2O species at defect-terrace and protrusion sites on the

defect, respectively. These studies demonstrated the strength of EC-TERS in nanoscale characterization of potential-driven reactions that are taking place battery materials or at electrocatalytic sites.

5.5 Catalysis at the nanoscale

TERS is also being used increasingly in catalysis research,[143,209–212] with the ultimate goal to obtain detailed chemical information of species at the catalyst's active sites. It has to be kept in mind that a plasmonic tip can itself exhibit catalytic activity: using TERS with a silver-coated AFM tip to both enhance the Raman signal and to act as the catalyst, van Schrojenstein Lantman *et al.* showed that time-resolved experiments can monitor photocatalytic reactions of a self-assembled monolayer of *p*-nitrothiophenol molecules adsorbed on gold nanoplates. A photocatalytic reduction process was induced at the apex of the tip by irradiation with green laser light, while red laser light was used to monitor the transformation process during the reaction.[213] Kumar *et al.* used the exact opposite strategy: they employed alumina protected TERS tips to study the oxidative dimerization of *p*-mercaptoaniline to *p*,*p*′-dimercaptoazobenzene on nanostructured silver,[214] and zirconia protected TERS tips to study photocatalytic reaction within an aqueous environment.[215]

Using TERS, Sun and co-workers showed that N=N bond of *p*,*p*′-dimercaptoazobisbenzene could be scissored by hot carriers with the formation of 4NTP at alkaline and *p*-aminothiophenol at acidic pH.[216] Szczerbinski and co-workers used TERS to monitor photocatalytic degradation of 1-hexadecanethiol, biphenyl-4-thiol and 1*H*,1*H*,2*H*,2*H*-perfluorodecane-1-thiol.[138] The researchers demonstrated that illumination of the tip–sample junction by high laser power (>1 mW) causes formation of carbonaceous species *via* charge-driven reaction mechanisms.

Su *et al.*, used TERS to map with high (≤2.5 nm) spatial resolution Pt nano-islands smaller than 10 nm on Au(111). The distinct Raman fingerprints 4-chlorophenyl isocyanide absorbed on a single nanoisland enabled resolving the electronic properties of the terrace, step edge, kink, and corner sites which are characterized by distinct coordination environments. Atomic sites with lower coordination numbers exhibited higher d-band electronic profiles which blue-shifted the N=C Raman frequency of the adsorbed 4-chlorophenyl isocyanide. An increasing number of Pt layers also weakened the influence of the underlying Au(111) surface (bimetallic effect).[217]

Recently, the Kurouski group reported on the sporadic formation of 4-nitrobenzenethiolate upon TERS imaging of a 4-nitrobenzenethiol (4NBT) monolayer on Au(111), Fig. 21. Using density functional theory (DFT), finite-difference time-domain (FDTD), and finite element method (FEM) calculations, Wang and co-workers concluded that this chemical transformation was not caused by plasmonic photothermal heating but was rather driven by plasmon-induced hot carriers.[218]

6. Differences, synergies, complementarity and future perspectives of TERS and AFM-IR

As mentioned in the introduction, although TERS and AFM-IR both leverage a scanning probe platform to overcome the light diffraction limit, they have evolved independently driven by different research priorities and by distinct underlying physical

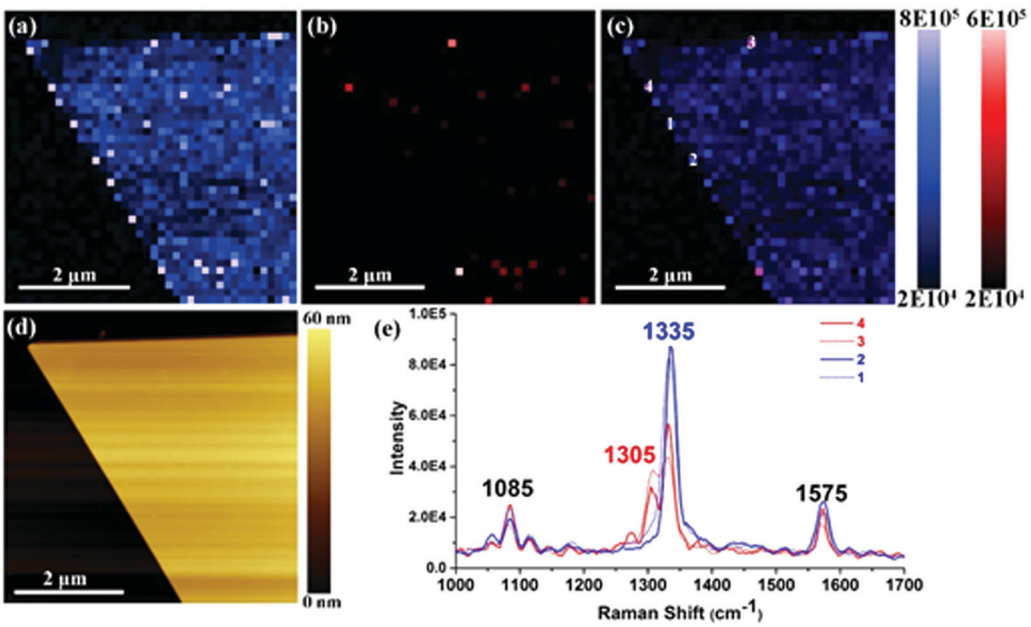

Fig. 21 TER images of a 4NBT monolayer on the gold Au (111) surface. (a) and (b) are based on the integral intensities of the spectrum from 1320 to 1350 cm^{-1} (a) and 1290 to 1320 cm^{-1} (b), respectively. (c) Overlapped image of (a) and (b). (d) The corresponding AFM image of the area where TER images were taken from. (e) Typical TERS spectra extracted from the marked position in (c). The scanning step is 20 nm per pixel. Reprinted with permission from Wang and Kurouski, *J. Phys. Chem. C*, 2020. Copyright (2020) American Chemical Society.

Table 2 Typical and best achieved characteristics of TERS and AFM-IR

	TERS		AFM-IR	
	Typical	Best achieved	Typical	Best achieved
Resolution achieved	3–5 nm	0.1 nm	10–50 nm	10 nm
Sampled depth	A few nm		A few μm	
Typical sample thickness			20–500 nm	
Sensitivity (smallest sample detected)	Single monolayer	Single molecule	20 nm thick	Single monolayer
Spectral range	500–1800 cm^{-1}	Unlimited	900–1900 cm^{-1} 2700–3600 cm^{-1}	20 000–625 cm^{-1} (limited by laser range)
Typical time for a spectrum	0.5–10 s	0.1 s	1–4 s (QCL) 1 min (OPO)	0.2 s
Spectral bandwidth	500–1800 cm^{-1} (but spectrometer dependent)		900–1900 cm^{-1}	5000–20 000 cm^{-1}
Spectral resolution	4–10 cm^{-1}		1 cm^{-1}	0.5 cm^{-1} (laser dependent)
Typical hyperspectral imaging & time	100 × 100 pixels (≈1.5–28 h)	—	100 × 100 pixels (≈3–11 h)	—
Typical pixel dwell time	0.5–10 s (equal to spectral acquisition time)		10 ms (single wavelength)	1 ms (single wavelength)
Reproducibility	Tip dependent		Tip independent but dependent on the tip–sample contact mechanics	
Spectral fidelity	High for small molecules, poor for complex biological samples		In first approximation, comparable to FTIR spectra	
Liquid measurement	Yes		Not typical	Achieved

mechanisms. However, the rapid pace of innovation for both techniques has pushed several measurement performance metrics well beyond initial expectations, opening new opportunities for synergistic TERS and AFM-IR characterization. Hereafter, we will highlight the major differences, complementarity, and possible areas of convergence between these two techniques. Table 2 summarized the typical and best achieved characteristics of TERS and AFM-IR.

The main difference between these two techniques is the extent of the sampled depth. While the TERS signal is typically generated from the top few nm of the sample, the sampling depth of AFM-IR can reach a few μm.[21] This single characteristic has been probably the main driver for the thus far limited application space overlap between AFM-IR and TERS, and together with the required spatial resolution, can be used as first discriminant for selecting the method most appropriate for a given application.

TERS is a surface sensitive technique because the TERS signal intensity and spatial resolution critically depends on the near-field enhancement conveyed by the scanning probe tip.[121,132] Consequently, experiment design (*i.e.* gap mode,[121,219] cryogenic temperature[133,142]) and tip engineering[220–222] to provide stronger and stronger near-fields has been a TERS research priority. The convergence of these intents has enabled TERS experimentalists to achieve a sub 0.1 nm spatial resolution at cryogenic temperatures,[223] much smaller that the tip-apex size limited resolution (*i.e.* 10 nm to 50 nm) suggested initially.[224] While the origin of such extreme spatial resolution is not well understood and subject of debate,[133] it enables molecular spectroscopy with unprecedented detail, although with low throughput. Imaging at 0.1 nm resolution requires sampling at twice the spatial frequency (*i.e.* 0.05 nm pixel size). Considering typical spectral acquisition times of 0.5 s for dye molecules and 10 s for proteins a 100 × 100 pixel map covering a 25 nm^2 area requires a little less than 1.5 h for dyes and more than a day for proteins (excluding the retrace time),[121,132] across a typical ≈1300 cm^{-1} bandwidth (from 500–1800 cm^{-1}). A wider TERS bandwidth can be achieved at the cost of lower resolution or by stitching different spectral ranges at the cost or longer measurement time. Claims for extraordinary spatial resolution require strong experimental and theoretical support, because in relation to the measurement time, thermal drift, thermal diffusion and tip stability present challenges for TERS imaging and reproducibility, especially at room temperature.[119] It is expected that a better theoretical understanding of the origin of TERS extreme spatial resolution will stimulate new tip designs and experimental strategies aimed at improving the measurement throughput, by increasing the signal-to-noise ratio (SNR). Alternatively, since such extreme spatial resolution is not always needed, tip engineering to achieve high SNR but across a wider area (*i.e.* with lower spatial resolution) is an interesting avenue

for improving throughput, reproducibility and enabling direct comparison with other lower-resolution nanoscale characterization methods, such as AFM-IR.[5,6]

The poor yield and the short life-time of TER probes is a serious issue that will have to be overcome to expand TERS application space and throughput.[225] Currently, silver- and gold-coated probes are commonly used in TERS because these metals have suitable dielectric constants in the visible range.[226] Although Au tips typically provide lower enhancement than Ag-tips, they are more stable (months) in air. In contrast, the oxidation of Ag by atmospheric oxygen or by sulfur-containing molecules quickly degrades Ag plasmonic activity.[227] Several strategies have been proposed to overcome this limitation. Specifically, the Zenobi group proposed to apply self-assemble monolayers of ethanethiolate to inhibit adsorption of contaminants, such as carbon and analyte molecules, on TERS tips.[221] This group also reported that plasmonic activity of contaminated tips could be restored by electrochemical reduction.[222] Independently, the Ren group demonstrated that sulfuric acid could be used to clean contaminated tips, restoring their plasmonic activity.[220] While TERS tips are typically custom fabricated in laboratory settings, we believed that commercial fabrication of TERS tips with high enhancement and long lifetimes will strongly foster the adoption of TERS. Also, stochastic fluctuations of bands can be observed in TERS. Probably diffusion and reorientation of molecules under the tip, as well as desorption, re-adsorption on the tip shaft and decomposition phenomena are at the basis of these spectral fluctuations. It was proposed that this could be due to molecule–metal interactions and incident light polarization.[179,228,229]

In contrast to TERS, AFM-IR does not require the field-enhancement of the tip and can measure the sample composition for depths even exceeding 1 μm,[21] leading to diverse applications but yielding no surface selectivity (*i.e.* for thick samples, the AFM-IR signal is contributed mostly by the sample subsurface). In principle, this distinction provides ground for a strong complementarity: surface composition by TERS and composition up to a few μm deep with AFM-IR; at least for TERS experiments that don't require the high sensitivity provided by the gap-mode excitation.

Since the field-enhancement is not crucial for AFM-IR, its development efforts have been primarily aimed at increasing sensitivity and throughput by resonant excitation of the cantilever oscillation either in contact-[13,28] or tapping-mode,[14–17] or by engineering more sensitive nanoscale probes.[19] While a TERS spectrum is acquired at once at each pixel, AFM-IR is typically a spectrally narrow-band measurement. OPO lasers have been used in AFM-IR across a broad spectral range, from 20 000 cm^{-1} (500 nm)[31] to 625 cm^{-1} (16 μm)[25] but have a slow wavelength tunability (typically 4 cm^{-1} s^{-1} to 40 cm^{-1} s^{-1}). The recent availability of quantum cascade lasers with fast wavelength tunability (>5000 cm^{-1} s^{-1}) and tunable repetition rate has considerably shortened the AFM-IR spectral acquisition time (≈ 1 s) enabling hyperspectral imaging at about 4 s per pixel (4 averaged spectra per pixel) across a ≈ 1000 cm^{-1} bandwidth, see Table 2. In these conditions, the typical AFM-IR hyperspectral imaging time (3 h to 11 h) is comparable with TERS. QCLs have also increased AFM-IR single wavelength chemical imaging throughput (≈ 10 ms per pixel). Considering the highest AFM-IR spatial resolution achieved in tapping-mode (≈ 10 nm),[15] a 5 nm pixel size and a 100 × 100 pixel single-wavelength map, covering an area of 2.5 μm^2, requires a little more than 3 min (excluding the retrace time). Consequently, AFM-IR single wavelength chemical imaging is fast and widespread while AFM-IR hyperspectral imaging has been rarely attempted.[60,99] Ultrasensitive optomechanical AFM probes[19] have the potential to improve the throughput further, at the cost of additional measurement complexity. An outstanding challenge for AFM-IR is the influence of the tip–sample contact dynamics on the AFM-IR signal intensities (scaling factor) that depends on the local thermomechanical properties of the sample and on the stability of the AFM operation. Such dependence makes quantification difficult, particularly for the more sensitive but less stable resonance enhanced excitation scheme[15] (see Section 2). While spectral ratios can be used, in first approximation, for semiquantitative assessments, the development of new highly-sensitive off-resonance methods[19,48] or methods that are immune to the scaling factor is highly desirable.[11]

Excluding the optomechanical probes,[19] and similarly to TERS, measuring the thinnest (monolayer) samples with AFM-IR typically requires a signal boost from the strong plasmonic enhancement occurring in the gap between a gold coated tip and a gold coated substrate.[13,38,39] AFM-IR measurements on such thin (<5 nm) samples are challenging but never the less they open up the possibility for spectroscopically complementary AFM-IR and TERS characterization on the same samples. While TERS measurements on monolayer or single molecules may be considered routine, AFM-IR measurement on these samples undoubtedly will benefit for an increase of the measurement resolution and sensitivity. *Ad hoc* engineering of the tip near-field in the mid-IR will probably be required to further this convergence and for pushing AFM-IR towards higher spatial resolution. Approaching the spatial resolution of TERS will require developing cryogenic AFM-IR instrumentation and exploiting the atomistic near-field enhancement as recently demonstrated in TERS.[132] Since IR absorption and Raman scattering are proportional to the second and forth power of the local electric field respectively, outside the atomistic near-field, for a given tip and sample it is otherwise expected that TERS will provide a higher spatial resolution than AFM-IR.

The comparison of recent applications of AFM-IR and TERS (Sections 3 and 5) suggests that for at least two areas, the characterization of 2D materials[39,63,198,230] and the characterization of biomolecular conformations[28,55,140,183] could benefit from the spectroscopic complementarity of these two techniques. Furthermore, the recent pioneering work in aqueous environment using both AFM-IR[28,29] and TERS,[146,203,205] highlights another emerging area of overlap that, however, will require further technical advances to impact a broad range of applications.

Given the vibrant TERS and AFM-IR research, we believe that innovations in probe fabrication, lasers and theory will aid further improvements in signal-to-noise ratio, and throughput of these techniques, enabling new applications and measurements in more extreme and diverse environmental conditions.

Conflicts of interest

The authors declare no competing financial interest.

References

1 M. Cardona, *Light Scattering in Solids*, Springer-Verlag, Berlin Heidelberg, 1975.
2 N. B. Colthup, L. H. Daly and S. E. Wiberley, *Introduction to Infrared and Raman Spectroscopy*, Academic Press, 1990.
3 C. Farber, J. Li, E. Hager, R. Chemelewski, J. Mullet, A. Y. Rogachev and D. Kurouski, *ACS Omega*, 2019, **4**, 3700–3707.
4 L. C. Prinsloo, W. du Plooy and C. van der Merwe, *J. Raman Spectrosc.*, 2004, **35**, 561–567.
5 A. Centrone, *Annu. Rev. Anal. Chem.*, 2015, **8**, 101–126.
6 A. Dazzi and C. B. Prater, *Chem. Rev.*, 2017, **117**, 5146–5173.
7 P. Verma, *Chem. Rev.*, 2017, **117**, 6447–6466.
8 T. Deckert-Gaudig, A. Taguchi, S. Kawata and V. Deckert, *Chem. Soc. Rev.*, 2017, **46**, 4077–4110.
9 M. Richard-Lacroix, Y. Zhang, Z. Dong and V. Deckert, *Chem. Soc. Rev.*, 2017, **46**, 3922–3944.
10 A. Dazzi, F. Glotin and R. Carminati, *J. Appl. Phys.*, 2010, **107**, 124519.
11 G. Ramer, V. A. Aksyuk and A. Centrone, *Anal. Chem.*, 2017, **89**, 13524–13531.
12 A. Dazzi, R. Prazeres, E. Glotin and J. M. Ortega, *Opt. Lett.*, 2005, **30**, 2388–2390.
13 F. Lu, M. Z. Jin and M. A. Belkin, *Nat. Photonics*, 2014, **8**, 307–312.
14 M. Tuteja, M. Kang, C. Leal and A. Centrone, *Analyst*, 2018, **143**, 3808–3813.
15 K. Wieland, G. Ramer, V. U. Weiss, G. Allmaier, B. Lendl and A. Centrone, *Nano Res.*, 2019, **12**, 197–203.
16 J. Mathurin, E. Pancani, A. Deniset-Besseau, K. Kjoller, C. B. Prater, R. Gref and A. Dazzi, *Analyst*, 2018, **143**, 5940–5949.
17 X. Ma, V. Beltran, G. Ramer, G. Pavlidis, D. Y. Parkinson, M. Thoury, T. Meldrum, A. Centrone and B. H. Berrie, *Angew. Chem., Int. Ed.*, 2019, **58**, 11652–11656.
18 L. Wang, H. Wang, M. Wagner, Y. Yan, D. S. Jakob and X. G. Xu, *Sci. Adv.*, 2017, **3**, e1700255.
19 J. Chae, S. An, G. Ramer, V. Stavila, G. Holland, Y. Yoon, A. A. Talin, M. Allendorf, V. A. Aksyuk and A. Centrone, *Nano Lett.*, 2017, **17**, 5587–5594.
20 A. Dazzi, in *Thermal Nanosystems and Nanomaterials*, ed. S. Volz, Springer Berlin, 2009, vol. 118, pp. 469–503.
21 B. Lahiri, G. Holland and A. Centrone, *Small*, 2013, **9**, 439–445.
22 F. Tang, P. Bao and Z. Su, *Anal. Chem.*, 2016, **88**, 4926–4930.
23 D. E. Barlow, J. C. Biffinger, A. L. Cockrell-Zugell, M. Lo, K. Kjoller, D. Cook, W. K. Lee, P. E. Pehrsson, W. J. Crookes-Goodson, C.-S. Hung, L. J. Nadeau and J. N. Russell, *Analyst*, 2016, **141**, 4848–4854.
24 J. Mathurin, E. Dartois, T. Pino, C. Engrand, J. Duprat, A. Deniset-Besseau, F. Borodnics, C. Sandt and A. Dazzi, *Astron. Astrophys.*, 2019, **622**, A160.
25 A. M. Katzenmeyer, V. Aksyuk and A. Centrone, *Anal. Chem.*, 2013, **85**, 1972–1979.
26 A. M. Katzenmeyer, J. Chae, R. Kasica, G. Holland, B. Lahiri and A. Centrone, *Adv. Opt. Mater.*, 2014, **2**, 718–722.
27 B. Lahiri, G. Holland, V. Aksyuk and A. Centrone, *Nano Lett.*, 2013, **13**, 3218–3224.
28 G. Ramer, F. S. Ruggeri, A. Levin, T. P. J. Knowles and A. Centrone, *ACS Nano*, 2018, **12**, 6612–6619.
29 M. Jin, F. Lu and M. A. Belkin, *Light: Sci. Appl.*, 2017, **6**, e17096.
30 C. Mayet, A. Dazzi, R. Prazeres, E. Allot, E. Glotin and J. M. Ortega, *Opt. Lett.*, 2008, **33**, 1611–1613.
31 A. M. Katzenmeyer, G. Holland, K. Kjoller and A. Centrone, *Anal. Chem.*, 2015, **87**, 3154–3159.
32 S. Clède, F. Lambert, C. Sandt, S. Kascakova, M. Unger, E. Harté, M.-A. Plamont, R. Saint-Fort, A. Deniset-Besseau, Z. Gueroui, C. Hirschmugl, S. Lecomte, A. Dazzi, A. Vessières and C. Policar, *Analyst*, 2013, **138**, 5627–5638.
33 A. Deniset-Besseau, C. B. Prater, M. J. Virolle and A. Dazzi, *J. Phys. Chem. Lett.*, 2014, **5**, 654–658.
34 A. Dazzi, C. B. Prater, Q. C. Hu, D. B. Chase, J. F. Rabolt and C. Marcott, *Appl. Spectrosc.*, 2012, **66**, 1365–1384.
35 J. Chae, B. Lahiri, J. Kohoutek, G. Holland, H. Lezec and A. Centrone, *Opt. Express*, 2015, **23**, 25912–25922.
36 C.-T. Wang, B. Jiang, Y.-W. Zhou, T.-W. Jiang, J.-H. Liu, G.-D. Zhu and W.-B. Cai, *Anal. Chem.*, 2019, **91**, 10541–10548.
37 K. Hinrichs and T. Shaykhutdinov, *Appl. Spectrosc.*, 2018, **72**, 817–832.
38 V. Giliberti, L. Baldassarre, A. Rosa, V. de Turris, M. Ortolani, P. Calvani and A. Nucara, *Nanoscale*, 2016, **8**, 17560–17567.
39 Z. L. Liu, K. Norgaard, M. H. Overgaard, M. Ceccato, D. M. A. Mackenzie, N. Stenger, S. L. S. Stipp and T. Hassenkam, *Carbon*, 2018, **127**, 141–148.
40 T. Shaykhutdinov, A. Furchner, J. Rappich and K. Hinrichs, *Opt. Mater. Express*, 2017, **7**, 3706–3714.
41 J. Chae, Q. Dong, J. Huang and A. Centrone, *Nano Lett.*, 2015, **15**, 8114–8121.
42 A. M. Katzenmeyer, G. Holland, J. Chae, A. Band, K. Kjoller and A. Centrone, *Nanoscale*, 2015, **7**, 17637–17641.
43 J. R. Felts, H. Cho, M. F. Yu, L. A. Bergman, A. F. Vakakis and W. P. King, *Rev. Sci. Instrum.*, 2013, **84**, 023709.
44 F. Lu and M. A. Belkin, *Opt. Express*, 2011, **19**, 19942–19947.
45 V. Giliberti, M. Badioli, A. Nucara, P. Calvani, E. Ritter, L. Puskar, E. F. Aziz, P. Hegemann, U. Schade, M. Ortolani and L. Baldassarre, *Small*, 2017, **13**, 1701181.
46 D. Partouche, J. Mathurin, A. Malabirade, S. Marco, C. Sandt, V. Arluison, A. Deniset-Besseau and S. Trepout, *J. Microsc.*, 2019, **274**, 23–31.

47 J. Waeytens, T. Doneux and S. Napolitano, *ACS Appl. Polym. Mater.*, 2019, **1**, 3–7.
48 S. Kenkel, A. Mittal, S. Mittal and R. Bhargava, *Anal. Chem.*, 2018, **90**, 8845–8855.
49 K. Kimura, K. Kobayashi, K. Matsushige and H. Yamada, *Ultramicroscopy*, 2013, **133**, 41–49.
50 L. Tetard, A. Passian and T. Thundat, *Nat. Nanotechnol.*, 2010, **5**, 105–109.
51 M. T. Cuberes, H. E. Assender, G. A. D. Briggs and O. V. Kolosov, *J. Phys. D: Appl. Phys.*, 2000, **33**, 2347–2355.
52 E. Pancani, J. Mathurin, S. Bilent, M. F. Bernet-Camard, A. Dazzi, A. Deniset-Besseau and R. Gref, *Part. Part. Syst. Charact.*, 2018, **35**, 1700457.
53 J. J. Schwartz, H.-J. Chuang, M. R. Rosenberger, S. V. Sivaram, K. M. McCreary, B. T. Jonker and A. Centrone, *ACS Appl. Mater. Interfaces*, 2019, **11**, 25578–25585.
54 A. M. Katzenmeyer, J. Canivet, G. Holland, D. Farrusseng and A. Centrone, *Angew. Chem., Int. Ed.*, 2014, **53**, 2852–2856.
55 F. S. Ruggeri, G. Longo, S. Faggiano, E. Lipiec, A. Pastore and G. Dietler, *Nat. Commun.*, 2015, **6**, 7831.
56 R. Rebois, D. Onidas, C. Marcott, I. Noda and A. Dazzi, *Anal. Bioanal. Chem.*, 2017, **409**, 2353–2361.
57 L. Gong, D. B. Chase, I. Noda, C. A. Marcott, J. Liu, D. C. Martin, C. Ni and J. F. Rabolt, *Macromolecules*, 2017, **50**, 5510–5517.
58 M. A. Rickard, G. F. Meyers, B. M. Habersberger, C. W. Reinhardt and J. J. Stanley, *Polymer*, 2017, **129**, 247–251.
59 S. Morsch, S. Lyon and S. R. Gibbon, *Prog. Org. Coat.*, 2017, **102**, 37–43.
60 K. Kochan, D. Perez-Guaita, J. Pissang, J. H. Jiang, A. Y. Peleg, D. McNaughton, P. Heraud and B. R. Wood, *J. R. Soc., Interface*, 2018, **15**, 20180115.
61 A. B. Khanikaev, N. Arju, Z. Fan, D. Purtseladze, F. Lu, J. Lee, P. Sarriugarte, M. Schnell, R. Hillenbrand, M. A. Belkin and G. Shvets, *Nat. Commun.*, 2016, **7**, 12045.
62 J. R. Felts, S. Law, C. M. Roberts, V. Podolskiy, D. M. Wasserman and W. P. King, *Appl. Phys. Lett.*, 2013, **102**, 152110.
63 L. V. Brown, M. Davanco, Z. Sun, A. Kretinin, Y. Chen, J. R. Matson, I. Vurgaftman, N. Sharac, A. J. Giles, M. M. Fogler, T. Taniguchi, K. Watanabe, K. S. Novoselov, S. A. Maier, A. Centrone and J. D. Caldwell, *Nano Lett.*, 2018, **18**, 1628–1636.
64 C. Ciano, V. Giliberti, M. Ortolani and L. Baldassarre, *Appl. Phys. Lett.*, 2018, **112**, 153101.
65 Y. Yoon, J. Chae, A. M. Katzenmeyer, H. P. Yoon, J. Schumacher, S. An, A. Centrone and N. Zhitenev, *Nanoscale*, 2017, **9**, 7771–7780.
66 E. Strelcov, Q. Dong, T. Li, J. Chae, Y. Shao, Y. Deng, A. Gruverman, J. Huang and A. Centrone, *Sci. Adv.*, 2017, **3**, e1602165.
67 S. Morsch, Y. W. Liu, S. B. Lyon and S. R. Gibbon, *ACS Appl. Mater. Interfaces*, 2016, **8**, 959–966.
68 Y. Yuan, J. Chae, Y. Shao, Q. Wang, Z. Xiao, A. Centrone and J. Huang, *Adv. Energy Mater.*, 2015, **5**, 1500615.
69 J. Chae, B. Lahiri and A. Centrone, *ACS Photonics*, 2016, **3**, 87–95.
70 V. Aksyuk, B. Lahiri, G. Holland and A. Centrone, *Nanoscale*, 2015, **7**, 3634–3644.
71 G. Delen, Z. Ristanovic, L. D. B. Mandemaker and B. M. Weckhuysen, *Chem. – Eur. J.*, 2018, **24**, 187–195.
72 C. Bartlam, S. Morsch, K. W. J. Heard, P. Quayle, S. G. Yeates and A. Vijayaraghavan, *Carbon*, 2018, **139**, 317–324.
73 H. S. Purohit and L. S. Taylor, *Mol. Pharmaceutics*, 2015, **12**, 4542–4553.
74 L. Imbert, S. Gourion-Arsiquaud, E. Villarreal-Ramirez, L. Spevak, H. Taleb, M. C. H. van der Meulen, R. Mendelsohn and A. L. Boskey, *PLoS One*, 2018, **13**, e0202833.
75 C. Farber, R. Wang, R. Chemelewski, J. Mullet and D. Kurouski, *Anal. Chem.*, 2019, **91**, 2472–2479.
76 J. Yang, J. Hatcherian, P. C. Hackley and A. E. Pomerantz, *Nat. Commun.*, 2017, **8**, 2179.
77 T. Hassenkam, M. P. Andersson, K. N. Dalby, D. M. A. Mackenzie and M. T. Rosing, *Nature*, 2017, **548**, 78–81.
78 A. L. Bondy, R. M. Kirpes, R. L. Merzel, K. A. Pratt, M. M. B. Holl and A. P. Ault, *Anal. Chem.*, 2017, **89**, 8594–8598.
79 S. Morsch, B. A. van Driel, K. J. van den Berg and J. Dik, *ACS Appl. Mater. Interfaces*, 2017, **9**, 10169–10179.
80 L. Xiao and Z. D. Schultz, *Anal. Chem.*, 2018, **90**, 440–458.
81 P. N. Tri and R. E. Prud'homme, *Macromolecules*, 2018, **51**, 181–188.
82 H. Furukawa, K. E. Cordova, M. O'Keeffe and O. M. Yaghi, *Science*, 2013, **341**, 1230444.
83 R. Dong, Y. Fang, J. Chae, J. Dai, Z. Xiao, Q. Dong, Y. Yuan, A. Centrone, X. C. Zeng and J. Huang, *Adv. Mater.*, 2015, **27**, 1912–1918.
84 M. A. Green, Y. Hishikawa, E. D. Dunlop, D. H. Levi, J. Hohl-Ebinger, M. Yoshita and A. W. Y. Ho-Baillie, *Prog. Photovoltaics*, 2019, **27**, 3–12.
85 H. J. Snaith, A. Abate, J. M. Ball, G. E. Eperon, T. Leijtens, N. K. Noel, S. D. Stranks, J. T. W. Wang, K. Wojciechowski and W. Zhang, *J. Phys. Chem. Lett.*, 2014, **5**, 1511–1515.
86 S. Colella, E. Mosconi, P. Fedeli, A. Listorti, F. Gazza, F. Orlandi, P. Ferro, T. Besagni, A. Rizzo and G. Calestani, *Chem. Mater.*, 2013, **25**, 4613–4618.
87 E. Gross, *Nano Res.*, 2019, **12**, 2200–2210.
88 A. Mancini, V. Giliberti, A. Alabastri, E. Calandrini, F. De Angelis, D. Garoli and M. Ortolani, *J. Phys. Chem. C*, 2018, **122**, 13072–13081.
89 P. Biagioni, J. S. Huang and B. Hecht, *Rep. Prog. Phys.*, 2012, **75**, 024402.
90 J. H. Park, G. von Maltzahn, L. L. Ong, A. Centrone, T. A. Hatton, E. Ruoslahti, S. N. Bhatia and M. J. Sailor, *Adv. Mater.*, 2010, **22**, 880–885.
91 J. D. Caldwell, L. Lindsey, V. Giannini, I. Vurgaftman, T. Reinecke, S. A. Maier and O. J. Glembocki, *Nanophotonics*, 2015, **4**, 44–68.
92 Z. Sun, Á. Gutiérrez-Rubio, D. N. Basov and M. M. Fogler, *Nano Lett.*, 2015, **15**, 4455–4460.
93 A. J. Giles, S. Dai, O. J. Glembocki, A. Kretinin, Z. Sun, C. Ellis, J. G. Tischler, T. Taniguchi, K. Watanabe,

M. M. Fogler, K. S. Novoselov, D. N. Basov and J. D. Caldwell, *Nano Lett.*, 2016, **16**, 3858–3865.
94 S. Z. Butler, S. M. Hollen, L. Y. Cao, Y. Cui, J. A. Gupta, H. R. Gutierrez, T. F. Heinz, S. S. Hong, J. X. Huang, A. F. Ismach, E. Johnston-Halperin, M. Kuno, V. V. Plashnitsa, R. D. Robinson, R. S. Ruoff, S. Salahuddin, J. Shan, L. Shi, M. G. Spencer, M. Terrones, W. Windl and J. E. Goldberger, *ACS Nano*, 2013, **7**, 2898–2926.
95 A. Dazzi, R. Prazeres, F. Glotin, J. M. Ortega, M. Al-Sawaftah and M. de Frutos, *Ultramicroscopy*, 2008, **108**, 635–641.
96 C. Mayet, A. Deniset-Besseau, R. Prazeres, J. M. Ortega and A. Dazzi, *Biotechnol. Adv.*, 2013, **31**, 369–374.
97 D. Khanal, A. Kondyurin, H. Hau, J. C. Knowles, O. Levinson, I. Ramzan, D. Fu, C. Marcott and W. Chrzanowski, *Anal. Chem.*, 2016, **88**, 7530–7538.
98 L. Quaroni, K. Pogoda, J. Wiltowska-Zuber and W. M. Kwiatek, *RSC Adv.*, 2018, **8**, 2786–2794.
99 D. Perez-Guaita, K. Kochan, M. Batty, C. Doerig, J. Garcia-Bustos, S. Espinoza, D. McNaughton, P. Heraud and B. R. Wood, *Anal. Chem.*, 2018, **90**, 3140–3148.
100 F. Chiti and C. M. Dobson, *Annu. Rev. Biochem.*, 2017, **86**, 27–68.
101 A. Barth, *Biochim. Biophys. Acta*, 2007, **1767**, 1073–1101.
102 F. S. Ruggeri, S. Vieweg, U. Cendrowska, G. Longo, A. Chiki, H. A. Lashuel and G. Dietler, *Sci. Rep.*, 2016, **6**, 31155.
103 C. Paluszkiewicz, N. Piergies, P. Chaniecki, M. Rekas, J. Miszczyk and W. M. Kwiatek, *J. Pharm. Biomed. Anal.*, 2017, **139**, 125–132.
104 N. Qin, S. Q. Zhang, J. J. Jiang, S. Gilbert Corder, Z. G. Qian, Z. T. Zhou, W. Lee, K. Y. Liu, X. H. Wang, X. X. Li, Z. F. Shi, Y. Mao, H. A. Bechtel, M. C. Martin, X. X. Xia, B. Marelli, D. L. Kaplan, F. G. Omenetto, M. K. Liu and T. H. Tao, *Nat. Commun.*, 2016, **7**, 13079.
105 S. Henry, N. B. Bercu, C. Bobo, C. Cullin, M. Molinari and S. Lecomte, *Nanoscale*, 2018, **10**, 936–940.
106 V. Giliberti, R. Polito, E. Ritter, M. Broser, P. Hegemann, L. Puskar, U. Schade, L. Zanetti-Polzi, I. Daidone, S. Corni, F. Rusconi, P. Biagioni, L. Baldassarre and M. Ortolani, *Nano Lett.*, 2019, **19**, 3104–3114.
107 Y. Kebukawa, H. Kobayashi, N. Urayama, N. Baden, M. Kondo, M. E. Zolensky and K. Kobayashi, *Proc. Natl. Acad. Sci. U. S. A.*, 2019, **116**, 753–758.
108 G. Latour, L. Robinet, A. Dazzi, F. Portier, A. Deniset-Besseau and M. C. Schanne-Klein, *Sci. Rep.*, 2016, **6**, 26344.
109 M. S. Anderson, *Appl. Phys. Lett.*, 2000, **76**, 3130–3132.
110 R. M. Stöckle, Y. D. Suh, V. Deckert and R. Zenobi, *Chem. Phys. Lett.*, 2000, **318**, 131–136.
111 N. Hayazawa, Y. Inouye, Z. Sekkat and S. Kawata, *Opt. Commun.*, 2000, **183**, 333–336.
112 S. L. Kleinman, R. R. Frontiera, A. I. Henry, J. A. Dieringer and R. P. Van Duyne, *Phys. Chem. Chem. Phys.*, 2013, **15**, 21–36.
113 B. Sharma, R. R. Frontiera, A. I. Henry, E. Ringe and R. P. Van Duyne, *Mater. Today*, 2012, **15**, 16–25.
114 R. J. Brown and M. J. T. Milton, *J. Raman Spectrosc.*, 2008, **39**, 1313–1326.
115 T. J. Antosiewicz and S. P. Apell, *RSC Adv.*, 2015, **5**, 6378–6384.
116 N. Zettsu, J. M. McLellan, B. Wiley, Y. Yin, Z. Y. Li and Y. Xia, *Angew. Chem., Int. Ed.*, 2006, **45**, 1288–1292.
117 K. Kim, K. L. Kim, H. B. Lee and K. S. Shin, *J. Phys. Chem. C*, 2010, **114**, 18679–18685.
118 B. Sharma, M. F. Cardinal, M. B. Ross, A. B. Zrimsek, S. V. Bykov, D. Punihaole, S. A. Asher, G. C. Schatz and R. P. Van Duyne, *Nano Lett.*, 2016, **16**, 7968–7973.
119 D. Kurouski, *Vib. Spectrosc.*, 2017, **91**, 3–15.
120 N. Jiang, E. T. Foley, J. M. Klingsporn, M. D. Sonntag, N. A. Valley, J. A. Dieringer, T. Seideman, G. C. Schatz, M. C. Hersam and R. P. Van Duyne, *Nano Lett.*, 2012, **12**, 5061–5067.
121 R. Wang and D. Kurouski, *J. Phys. Chem. C*, 2018, **122**, 24334–24340.
122 T. Deckert-Gaudig, E. Kämmer and V. Deckert, *J. Biophotonics*, 2012, **5**, 215–219.
123 E. Sheremet, R. D. Rodriguez, D. R. T. Zahn, A. G. Milekhin, E. E. Rodyakina and A. V. Latyshev, *J. Vac. Sci. Technol., B*, 2014, **32**, 04E109.
124 L. Gao, H. Zhao, Y. Li, T. Li, D. Chen and B. Liu, *Nanoscale Res. Lett.*, 2018, **13**, 366.
125 N. Martín Sabanés, L. M. A. Driessen and K. F. Domke, *Anal. Chem.*, 2016, **88**, 7108–7114.
126 N. Martin Sabanes, T. Ohto, D. Andrienko, Y. Nagata and K. F. Domke, *Angew. Chem., Int. Ed.*, 2017, **56**, 9796–9801.
127 Z. C. Zeng, S. C. Huang, D. Y. Wu, L. Y. Meng, M. H. Li, T. X. Huang, J. H. Zhong, X. Wang, Z. L. Yang and B. Ren, *J. Am. Chem. Soc.*, 2015, **137**, 11928–11931.
128 F. De Angelis, G. Das, P. Candeloro, M. Patrini, M. Galli, A. Bek, M. Lazzarino, I. Maksymov, C. Liberale, L. C. Andreani, E. Di Fabrizio and C. Ellis, *Nat. Nanotechnol.*, 2010, **5**, 67–72.
129 A. Bek, F. De Angelis, G. Das, E. Di Fabrizio and M. Lazzarino, *Micron*, 2011, **42**, 313–317.
130 S. F. Becker, M. Esmann, K. Yoo, P. Gross, R. Vogelgesang, N. Park and C. Lienau, *ACS Photonics*, 2016, **3**, 223–232.
131 S. Trautmann, J. Aizpurua, I. Gotz, A. Undisz, J. Dellith, H. Schneidewind, M. Rettenmayr and V. Deckert, *Nanoscale*, 2017, **9**, 391–401.
132 J. Lee, K. T. Crampton, N. Tallarida and V. A. Apkarian, *Nature*, 2019, **568**, 78–82.
133 R. Zhang, Y. Zhang, Z. C. Dong, S. Jiang, C. Zhang, L. G. Chen, L. Zhang, Y. Liao, J. Aizpurua, Y. Luo, J. L. Yang and J. G. Hou, *Nature*, 2013, **498**, 82–86.
134 P. Roelli, C. Galland, N. Piro and T. J. Kippenberg, *Nat. Nanotechnol.*, 2015, **11**, 164.
135 Y. Zhang, D. V. Voronine, S. Qiu, A. M. Sinyukov, M. Hamilton, Z. Liege, A. V. Sokolov, Z. Zhang and M. O. Scully, *Sci. Rep.*, 2016, **6**, 25788.
136 S. S. Masango, R. A. Hackler, N. Large, A. I. Henry, M. O. McAnally, G. C. Schatz, P. C. Stair and R. P. Van Duyne, *Nano Lett.*, 2016, **16**, 4251–4259.
137 D. Kurouski, T. Postiglione, T. Deckert-Gaudig, V. Deckert and I. K. Lednev, *Analyst*, 2013, **138**, 1665–1673.
138 J. Szczerbinski, L. Gyr, J. Kaeslin and R. Zenobi, *Nano Lett.*, 2018, **18**, 6740–6749.

139 N. Valley, N. Greeneltch, R. P. Van Duyne and G. C. Schatz, *J. Phys. Chem. Lett.*, 2013, **4**, 2599–2604.
140 D. Kurouski, T. Deckert-Gaudig, V. Deckert and I. K. Lednev, *J. Am. Chem. Soc.*, 2012, **134**, 13323–13329.
141 T. Touzalin, A. L. Dauphin, S. Joiret, I. T. Lucas and E. Maisonhaute, *Phys. Chem. Chem. Phys.*, 2016, **18**, 15510–15513.
142 J. M. Klingsporn, N. Jiang, E. A. Pozzi, M. D. Sonntag, D. Chulhai, T. Seideman, L. Jensen, M. C. Hersam and R. P. Van Duyne, *J. Am. Chem. Soc.*, 2014, **136**, 3881–3887.
143 J. H. Zhong, X. Jin, L. Meng, X. Wang, H. S. Su, Z. L. Yang, C. T. Williams and B. Ren, *Nat. Nanotechnol.*, 2017, **12**, 132–136.
144 N. Chiang, X. Chen, G. Goubert, D. V. Chulhai, X. Chen, E. A. Pozzi, N. Jiang, M. C. Hersam, T. Seideman, L. Jensen and R. P. Van Duyne, *Nano Lett.*, 2016, **16**, 7774–7778.
145 D. Zhang, X. Wang, K. Braun, H.-J. Egelhaaf, M. Fleischer, L. Hennemann, H. Hintz, C. Stanicu, C. J. Brabec, D. P. Kern and A. J. Meixner, *J. Raman Spectrosc.*, 2009, **40**, 1371–1376.
146 T. Touzalin, S. Joiret, E. Maisonhaute and I. T. Lucas, *Anal. Chem.*, 2017, **89**, 8974–8980.
147 R. Treffer, R. Bohme, T. Deckert-Gaudig, K. Lau, S. Tiede, X. Lin and V. Deckert, *Biochem. Soc. Trans.*, 2012, **40**, 609–614.
148 R. Treffer and V. Deckert, *Curr. Opin. Biotechnol.*, 2010, **21**, 4–11.
149 E. Lipiec, D. Perez-Guaita, J. Kaderli, B. R. Wood and R. Zenobi, *Angew. Chem., Int. Ed.*, 2018, **57**, 8519–8524.
150 E. A. Pozzi, M. D. Sonntag, N. Jiang, N. Chiang, T. Seideman, M. C. Hersam and R. P. Van Duyne, *J. Phys. Chem. Lett.*, 2014, **5**, 2657–2661.
151 J. M. Klingsporn, M. D. Sonntag, T. Seideman and R. P. Van Duyne, *J. Phys. Chem. Lett.*, 2014, **5**, 106–110.
152 A. Jorio, L. G. Cançado, S. Heeg, L. Novotny and A. Hartschuh, in *Handbook of Carbon Nanomaterials*, ed. R. B. Weismann and J. Kono, World Scientific, New York, 2019, vol. 10, Optical Properties of Carbon Nanotubes, Part II: A Volume Dedicated to the Memory of Professor Mildred S Dresselhaus, pp. 175–221.
153 M. D. Sonntag, J. M. Klingsporn, L. Garibay, D. Roberts, J. A. Dieringer, K. A. Scheidt, L. Jensen, G. C. Schatz, T. Seideman and R. P. Van Duyne, *J. Phys. Chem. C*, 2012, **116**, 478–483.
154 T. Deckert-Gaudig, A. Taguchi, S. Kawata and V. Deckert, *Chem. Soc. Rev.*, 2017, **46**, 4077–4110.
155 D. Kurouski, S. Zaleski, F. Casadio, R. P. Van Duyne and N. C. Shah, *J. Am. Chem. Soc.*, 2014, **136**, 8677–8684.
156 F. Pashaee, R. Hou, P. Gobbo, M. S. Workentin and F. Lagugné-Labarthet, *J. Phys. Chem. C*, 2013, **117**, 15639–15646.
157 B. Pettinger, B. Ren, G. Picardi, R. Schuster and G. Ertl, *Phys. Rev. Lett.*, 2004, **92**, 096101.
158 C. Chen, N. Hayazawa and S. Kawata, *Nat. Commun.*, 2014, **5**, 3312.
159 R. Zhang, X. Zhang, H. Wang, Y. Zhang, S. Jiang, C. Hu, Y. Zhang, Y. Luo and Z. Dong, *Angew. Chem., Int. Ed.*, 2017, **56**, 5561–5564.
160 N. Tallarida, J. Lee and V. A. Apkarian, *ACS Nano*, 2017, **11**, 11393–11401.
161 X.-M. Lin, T. Deckert-Gaudig, P. Singh, M. Siegmann, S. Kupfer, Z. Zhang, S. Grafe and V. Deckert, 2016, arXiv:1604.06598.
162 Z. He, Z. Han, M. Kizer, R. J. Linhardt, X. Wang, A. M. Sinyukov, J. Wang, V. Deckert, A. V. Sokolov, J. Hu and M. O. Scully, *J. Am. Chem. Soc.*, 2019, **141**, 753–757.
163 E. Agosti, M. Rivola, V. Hernandez, M. Del Zoppo and G. Zerbi, *Synth. Met.*, 1999, **100**, 101–112.
164 A. Alu and N. Engheta, *Phys. Rev. Lett.*, 2009, **103**, 143902.
165 C. Gullekson, L. Lucas, K. Hewitt and L. Kreplak, *Biophys. J.*, 2011, **100**, 1837–1845.
166 R. Treffer, X. Lin, E. Bailo, T. Deckert-Gaudig and V. Deckert, *Beilstein J. Nanotechnol.*, 2011, **2**, 628–637.
167 A. Rasmussen and V. Deckert, *J. Raman Spectrosc.*, 2006, **37**, 311–317.
168 S. Naijar, D. Talaga, L. Schué, Y. Coffinier, S. Szunerits, R. Boukherroub, L. Servant, V. Rodriguez and S. Bonhommeau, *J. Phys. Chem. C*, 2014, **118**, 1174–1181.
169 F. Pashaee, M. Tabatabaei, F. A. Caetano, S. S. Ferguson and F. Lagugne-Labarthet, *Analyst*, 2016, **141**, 3251–3258.
170 E. Lipiec, R. Sekine, J. Bielecki, W. M. Kwiatek and B. R. Wood, *Angew. Chem., Int. Ed.*, 2014, **53**, 169–172.
171 T. P. Knowles, M. Vendruscolo and C. M. Dobson, *Nat. Rev.*, 2014, **15**, 384–396.
172 T. Deckert-Gaudig, D. Kurouski, M. A. Hedegaard, P. Singh, I. K. Lednev and V. Deckert, *Sci. Rep.*, 2016, **6**, 33575.
173 S. Bonhommeau, D. Talaga, J. Hunel, C. Cullin and S. Lecomte, *Angew. Chem., Int. Ed.*, 2017, **56**, 1771–1774.
174 C. C. vandenAkker, T. Deckert-Gaudig, M. Schleeger, K. P. Velikov, V. Deckert, M. Bonn and G. H. Koenderink, *Small*, 2015, **11**, 4131–4139.
175 M. Tabatabaei, F. A. Caetano, F. Pashee, S. S. G. Ferguson and F. Lagugne-Labarthet, *Analyst*, 2017, **142**, 4415–4421.
176 D. Kurouski, R. A. Lombardi, R. K. Dukor, I. K. Lednev and L. A. Nafie, *Chem. Commun.*, 2010, **46**, 7154–7156.
177 D. Kurouski, R. P. Van Duyne and I. K. Lednev, *Analyst*, 2015, **140**, 4967–4980.
178 D. Kurouski, R. K. Dukor, X. Lu, L. A. Nafie and I. K. Lednev, *Biophys. J.*, 2012, **103**, 522–531.
179 S. Srinivasan, S. Patke, Y. Wang, Z. Ye, J. Litt, S. K. Srivastava, M. M. Lopez, D. Kurouski, I. K. Lednev, R. S. Kane and W. Colon, *J. Biol. Chem.*, 2013, **288**, 2744–2755.
180 D. Kurouski, T. Deckert-Gaudig, V. Deckert and I. K. Lednev, *Biophys. J.*, 2014, **106**, 263–271.
181 A. V. Krasnoslobodtsev, T. Deckert-Gaudig, Y. Zhang, V. Deckert and Y. L. Lyubchenko, *Ultramicroscopy*, 2016, **165**, 26–33.
182 B. R. Wood, E. Bailo, M. A. Khiavi, L. Tilley, S. Deed, T. Deckert-Gaudig, D. McNaughton and V. Deckert, *Nano Lett.*, 2011, **11**, 1868–1873.
183 R. Bohme, M. Mkandawire, U. Krause-Buchholz, P. Rosch, G. Rodel, J. Popp and V. Deckert, *Chem. Commun.*, 2011, **47**, 11453–11455.

184 L. Xiao, K. A. Bailey, H. Wang and Z. D. Schultz, *Anal. Chem.*, 2017, **89**, 9091–9099.
185 A. C. Ferrari, J. C. Meyer, V. Scardaci, C. Casiraghi, M. Lazzeri, F. Mauri, S. Piscanec, D. Jiang, K. S. Novoselov, S. Roth and A. K. Geim, *Phys. Rev. Lett.*, 2006, **97**, 187401.
186 R. Zhao, Y. Zhang, T. Gao, Y. Gao, N. Liu, L. Fu and Z. Liu, *Nano Res.*, 2011, **4**, 712–721.
187 J. Stadler, T. Schmid and R. Zenobi, *ACS Nano*, 2011, **5**, 8442–8448.
188 F. Schaffel, M. Wilson, A. Bachmatiuk, M. H. Rummeli, U. Queitsch, B. Rellinghaus, G. A. Briggs and J. H. Warner, *ACS Nano*, 2011, **5**, 1975–1983.
189 K. F. Domke and B. Pettinger, *J. Raman Spectrosc.*, 2009, **40**, 1427–1433.
190 W. Su, N. Kumar, A. Krayev and M. Chaigneau, *Nat. Commun.*, 2018, **9**, 2891.
191 A. G. Milekhin, M. Rahaman, E. E. Rodyakina, A. V. Latyshev, V. M. Dzhagan and D. R. T. Zahn, *Nanoscale*, 2018, **10**, 2755–2763.
192 F. Shao and R. Zenobi, *Anal. Bioanal. Chem.*, 2018, 1–25.
193 F. Shao, V. Müller, Y. Zhang, A. D. Schlüter and R. Zenobi, *Angew. Chem., Int. Ed.*, 2017, **56**, 9361–9366.
194 M. Servalli, L.-Q. Zheng, R. Zenobi and A. D. Schlüter, *ACS Nano*, 2018, **12**, 11294–11306.
195 L. Opilik, P. Payamyar, J. Szczerbinski, A. P. Schutz, M. Servalli, T. Hungerland, A. D. Schluter and R. Zenobi, *ACS Nano*, 2015, **9**, 4252–4259.
196 V. Müller, F. Shao, M. Baljozovic, M. Moradi, Y. Zhang, T. Jung, W. B. Thompson, B. T. King, R. Zenobi and A. D. Schlüter, *Angew. Chem., Int. Ed.*, 2017, **56**, 15262–15266.
197 W. Dai, F. Shao, J. Szczerbiński, R. McCaffrey, R. Zenobi, Y. Jin, A. D. Schlüter and W. Zhang, *Angew. Chem., Int. Ed.*, 2016, **128**, 221–225.
198 F. Shao, W. Dai, Y. Zhang, W. Zhang, A. D. Schlüter and R. Zenobi, *ACS Nano*, 2018, **12**, 5021–5029.
199 D. Wang and L.-J. Wan, *J. Phys. Chem. C*, 2007, **111**, 16109–16130.
200 S. Yoshimoto and K. Itaya, *Annu. Rev. Anal. Chem.*, 2013, **6**, 213–235.
201 A. J. Bard, F. R. F. Fan, J. Kwak and O. Lev, *Anal. Chem.*, 1989, **61**, 132–138.
202 T. Sun, Y. Yu, B. J. Zacher and M. V. Mirkin, *Angew. Chem., Int. Ed.*, 2014, **53**, 14120–14123.
203 D. Kurouski, M. Mattei and R. P. Van Duyne, *Nano Lett.*, 2015, **15**, 7956–7962.
204 M. Mattei, G. Kang, G. Goubert, D. V. Chulhai, G. C. Schatz, L. Jensen and R. P. Van Duyne, *Nano Lett.*, 2017, **17**, 590–596.
205 G. Kang, M. Yang, M. S. Mattei, G. C. Schatz and R. P. Van Duyne, *Nano Lett.*, 2019, **19**, 2106–2113.
206 S. C. Huang, J. Z. Ye, X. R. Shen, Q. Q. Zhao, Z. C. Zeng, M. H. Li, D. Y. Wu, X. Wang and B. Ren, *Anal. Chem.*, 2019, **91**, 11092–11097.
207 T. Touzalin, S. Joiret, I. T. Lucas and E. Maisonhaute, *Electrochem. Commun.*, 2019, **108**, 106557.
208 J. H. K. Pfisterer, M. Baghernejad, G. Giuzio and K. F. Domke, *Nat. Commun.*, 2019, **10**, 5702.
209 T. Hartman, C. S. Wondergem, N. Kumar, A. van den Berg and B. M. Weckhuysen, *J. Phys. Chem. Lett.*, 2016, **7**, 1570–1584.
210 J. G. Wang, W. H. Qiao and X. J. Mu, *Appl. Sci.*, 2018, **8**, 15.
211 A. B. Zrimsek, N. H. Chiang, M. Mattei, S. Zaleski, M. O. McAnally, C. T. Chapman, A. I. Henry, G. C. Schatz and R. P. Van Duyne, *Chem. Rev.*, 2017, **117**, 7583–7613.
212 S. Dery, E. Amit and E. Gross, *Top. Catal.*, 2018, **61**, 923–939.
213 E. M. van Schrojenstein Lantman, T. Deckert-Gaudig, A. J. G. Mank, V. Deckert and B. M. Weckhuysen, *Nat. Nanotechnol.*, 2012, **7**, 583–586.
214 N. Kumar, B. Stephanidis, R. Zenobi, A. J. Wain and D. Roy, *Nanoscale*, 2015, **7**, 7133–7137.
215 N. Kumar, C. S. Wondergem, A. J. Wain and B. M. Weckhuysen, *J. Phys. Chem. Lett.*, 2019, **10**, 1669–1675.
216 M. Sun, Z. Zhang, Z. H. Kim, H. Zheng and H. Xu, *Chemistry*, 2013, **19**, 14958–14962.
217 H. S. Su, X. G. Zhang, J. J. Sun, X. Jin, D. Y. Wu, X. B. Lian, J. H. Zhong and B. Ren, *Angew. Chem., Int. Ed.*, 2018, **57**, 13177–13181.
218 R. Wang, J. Li, J. Rigor, N. Large, P. El-Khoury, A. Y. Rogachev and D. Kurouski, *J. Phys. Chem. C*, 2020, **124**, 2238–2244.
219 S. Mahapatra, Y. Ning, J. F. Schultz, L. Li, J. L. Zhang and N. Jiang, *Nano Lett.*, 2019, **19**, 3267–3272.
220 B. Ren, G. Picardi, B. Pettinger, R. Schuster and G. Ertl, *Angew. Chem., Int. Ed.*, 2005, **44**, 139–142.
221 T. Schmid, B. S. Yeo, G. Leong, J. Stadler and R. Zenobi, *J. Raman Spectrosc.*, 2009, **40**, 1392–1399.
222 L. Opilik, Ü. Dogan, J. Szczerbiński and R. Zenobi, *Appl. Phys. Lett.*, 2015, **107**, 091109.
223 J. Lee, K. T. Crampton, N. Tallarida and V. A. Apkarian, *Nature*, 2019, **568**, 78–82.
224 R. M. Stöckle, Y. D. Suh, V. Deckert and R. Zenobi, *Chem. Phys. Lett.*, 2000, **318**, 131–136.
225 T. X. Huang, S. C. Huang, M. H. Li, Z. C. Zeng, X. Wang and B. Ren, *Anal. Bioanal. Chem.*, 2015, **407**, 8177–8195.
226 E. D. Palik, *Handbook of optical constants of solids III*, Academic Press, New York, 1998.
227 L. Opilik, Ü. Dogan, J. Szczerbiński and R. Zenobi, *Appl. Phys. Lett.*, 2015, **107**, 091109.
228 M. D. Sonntag, D. Chulhai, T. Seideman, L. Jensen and R. P. Van Duyne, *J. Am. Chem. Soc.*, 2013, **135**, 17187–17192.
229 V. Deckert, T. Deckert-Gaudig, M. Diegel, I. Gotz, L. Langeluddecke, H. Schneidewind, G. Sharma, P. Singh, P. Singh, S. Trautmann, M. Zeisberger and Z. Zhang, *Faraday Discuss.*, 2015, **177**, 9–20.
230 L. Q. Zheng, X. Wang, F. Shao, M. Hegner and R. Zenobi, *Angew. Chem., Int. Ed.*, 2018, **57**, 1025–1029.